



HAL
open science

Influence of the Lode parameter and the stress triaxiality on the failure of elasto-plastic porous materials

Kostas Danas, Pedro Ponte Castañeda

► To cite this version:

Kostas Danas, Pedro Ponte Castañeda. Influence of the Lode parameter and the stress triaxiality on the failure of elasto-plastic porous materials. *International Journal of Solids and Structures*, 2012, 49, pp.1325-1342. hal-00755852

HAL Id: hal-00755852

<https://polytechnique.hal.science/hal-00755852>

Submitted on 22 Dec 2017

HAL is a multi-disciplinary open access archive for the deposit and dissemination of scientific research documents, whether they are published or not. The documents may come from teaching and research institutions in France or abroad, or from public or private research centers.

L'archive ouverte pluridisciplinaire **HAL**, est destinée au dépôt et à la diffusion de documents scientifiques de niveau recherche, publiés ou non, émanant des établissements d'enseignement et de recherche français ou étrangers, des laboratoires publics ou privés.

Influence of the Lode parameter and the stress triaxiality on the failure of elasto-plastic porous materials

K. Danas^{a,*}, P. Ponte Castañeda^{b,c}

^aLaboratoire de Mécanique des Solides, C.N.R.S. UMR7649, École Polytechnique, 91128 Palaiseau Cedex, France

^bDepartment of Mechanical Engineering and Applied Mechanics, University of Pennsylvania, Philadelphia, PA 19104-6315, U.S.A.

^cMadrid Institute for Advanced Studies of Materials (IMDEA-Materials), 28040 Madrid, Spain

Abstract

This work makes use of a recently developed “second-order” homogenization model to investigate failure in porous elasto-plastic solids under general triaxial loading conditions. The model incorporates dependence on the porosity and average pore shape, whose evolution is sensitive to the stress triaxiality and Lode parameter L . For positive triaxiality (with overall tensile hydrostatic stress), two different macroscopic failure mechanisms are possible, depending on the level of the triaxiality. At high triaxiality, void growth induces softening of the material, which overtakes the intrinsic strain hardening of the matrix phase, leading to a maximum in the effective stress-strain relation for the porous material, followed by loss of ellipticity by means of dilatant shear localization bands. In this regime, the ductility decreases with increasing triaxiality and is weakly dependent on the Lode parameter, in agreement with earlier theoretical analyses and experimental observations. At low triaxiality, however, a new mechanism comes into play consisting in the abrupt collapse of the voids along a compressive direction (with small, but finite porosity), which can dramatically soften the response of the porous material, leading to a sudden drop in its load-carrying capacity, and to loss of ellipticity of its incremental constitutive relation through localization of deformation. This low-triaxiality failure mechanism leads to a reduction in the ductility of the material as the triaxiality decreases to zero, and is highly dependent on the value of the Lode parameter. Thus, while no void collapse is observed at low triaxiality for axisymmetric tension ($L = -1$), the ductility of the material drops sharply with decreasing values of the Lode parameter, and is smallest for biaxial tension with axisymmetric compression ($L = +1$). In addition, the model predicts a sharp transition from the low-triaxiality regime, with increasing ductility, to the high-triaxiality regime, with decreasing ductility, as the failure mechanism switches from void collapse to void growth, and is in qualitative agreement with recent experimental work.

Key words: Plasticity, Void Growth, Porous materials, Lode parameter, Shear Localization, Homogenization, Microstructure evolution

1. Introduction

Due to its critical technological importance, ductile failure and fracture of metallic materials has been the focus of continued attention over the last sixty years. The main mechanism for material failure in ductile solids is the nucleation, growth and eventual coalesce of voids and micro-cracks as a result of the applied loading conditions (Garrison and Moody, 1987). It has been known for many years that the stress triaxiality, denoted here by X_Σ and defined as the ratio of the mean stress to the von Mises equivalent or effective deviatoric stress, is the critical parameter controlling ductile failure at high triaxiality. Thus, large amounts of experimental data (Hancock and Mackenzie, 1976; Le Roy et al., 1981; Johnson and Cook, 1985)

*Corresponding author.

Email addresses: kdanas@lms.polytechnique.fr (K. Danas), ponte@seas.upenn.edu (P. Ponte Castañeda)

39 have shown a monotonic decrease of material ductility with increasing stress triaxiality. This is consistent
 40 with the expected increase in the rate of growth of the voids with a larger tensile hydrostatic stress compo-
 41 nent. Nonetheless, recent experimental evidence (Bao and Wierzbicki, 2004; Barsoum and Faleskog, 2007a;
 42 Mohr and Ebnoether, 2009; Dunand and Mohr, 2010) suggests that a new, different mechanism should come
 43 into play at low triaxialities, leading to a substantial reduction of the material ductility with *decreasing* stress
 44 triaxiality. Indeed, in these studies, it has been found that a second loading parameter, the Lode parameter,
 45 L (or equivalently Lode angle, θ) also plays a significant role in ductile failure at low stress triaxialities. The
 46 Lode parameter is a function of the third invariant of the stress deviator and is used to distinguish between
 47 the different shear stress states in three dimensions (3-D), ranging from axisymmetric tension to biaxial
 48 tension with axisymmetric compression and passing through in-plane shear. The key experimental observa-
 49 tions are summarized in Fig. 1, which is taken from the work of Barsoum and Faleskog (2007a). Specifically,
 50 Fig. 1a shows the low-triaxiality regime with increasing ductility as the triaxiality increases, followed by an
 51 abrupt transition to the standard high-triaxiality regime with the opposite trend. Correspondingly, Figs. 1b,
 52 c and d show SEM micrographs of the failure surfaces for low, intermediate and high triaxiality. At low stress
 53 triaxialities (Fig. 1b), the dimples are shallow and elongated suggesting significant shear plastic strains and
 54 void elongation, together with shear localization between voids. At high stress triaxialities (Fig. 1d), the
 55 dimples are deep suggesting the well-known void coalescence mechanism with necking of inter-void ligaments
 56 leading to final rupture. At an intermediate value of the stress triaxiality ($X_{\Sigma} \approx 0.7 - 0.8$), a transition be-
 57 tween the void shearing and void growth mechanisms is observed. In conclusion, these careful experimental
 58 observations strongly suggest that, void elongation (with significant changes in shape), which is dependent
 59 on the specific shear stress state (as measured by the Lode parameter), becomes the dominant mechanism
 60 leading to the failure of the material at low stress triaxialities, and should therefore be accounted for in the
 61 constitutive modeling of such material systems.

62 The underlying microstructural mechanism at large triaxialities (i.e., large mean stresses compared to
 63 the deviatoric ones) was identified early on by McClintock (1968) and Rice and Tracey (1969), who related it
 64 to the growth of pre-existing voids or/and nucleated micro-voids mainly due to the presence of impurities in
 65 the material. This knowledge led to the development of the well-known Gurson (1977) model (and its modi-
 66 fications by Tvergaard (1981)) which is based on a micromechanical analysis of a spherical shell, assumed to
 67 remain spherical even for general loading conditions. However, while this assumption is entirely consistent
 68 with the void growth mechanisms observed under pure hydrostatic stress states, as already noted, it becomes
 69 less adequate with the addition of shear loads, since such loads can induce significant changes in the void
 70 shape. Early studies of the effect of triaxiality on void growth, accounting for shape changes, as well as its
 71 implications for ductile failure, were carried out by McClintock (1968, 1971) and Budiansky et al. (1982)
 72 (see also Teirlinck et al. (1988)). Building on these early works and on the works of Duvá and Hutchinson
 73 (1984) and Lee and Mear (1992), Gologanu et al. (1993, 1994) proposed a model for porous materials with
 74 aligned spheroidal voids that are subjected to axisymmetric stress states aligned with the voids symmetry
 75 axis. These Gurson-type models have been further developed by Gologanu et al. (1997), Gărăjeu et al.
 76 (2000), Pardoén and Hutchinson (2000), Benzerga (2002), Flandi and Leblond (2005a), Monchiet et al.
 77 (2007), Benzerga and Leblond (2010) and Keralavarma and Benzerga (2010) to account for more general
 78 loading conditions (and anisotropic matrix behavior in the case of Keralavarma and Benzerga (2010)), but
 79 still make the rather strong approximation that the voids remain *spheroidal* in shape for general triaxial
 80 loading histories.

81 A different class of constitutive models for porous viscoplastic materials capable of accounting for
 82 more general (i.e., arbitrary ellipsoidal) pore shape and orientation evolution have been developed by
 83 Ponte Castañeda and Zaidman (1994), Kailasam et al. (1997a) and Kailasam and Ponte Castañeda (1997)
 84 to deal with completely general, three-dimensional loading conditions. These models make use of the
 85 “variational linear comparison” homogenization method of Ponte Castañeda (1991) (see also Willis (1991),
 86 Michel and Suquet (1992)), together with the estimates of Ponte Castañeda and Willis (1995) for porous
 87 linear-elastic materials with “ellipsoidal” microstructures (i.e., particulate microstructures containing or-
 88 thotropic distributions of ellipsoidal pores), to generate corresponding estimates for the dissipation potential
 89 of the viscoplastic porous materials. They are supplemented by evolution laws for microstructural variables
 90 corresponding to the porosity, average pore shape and orientation, which are obtained from the homogeniza-

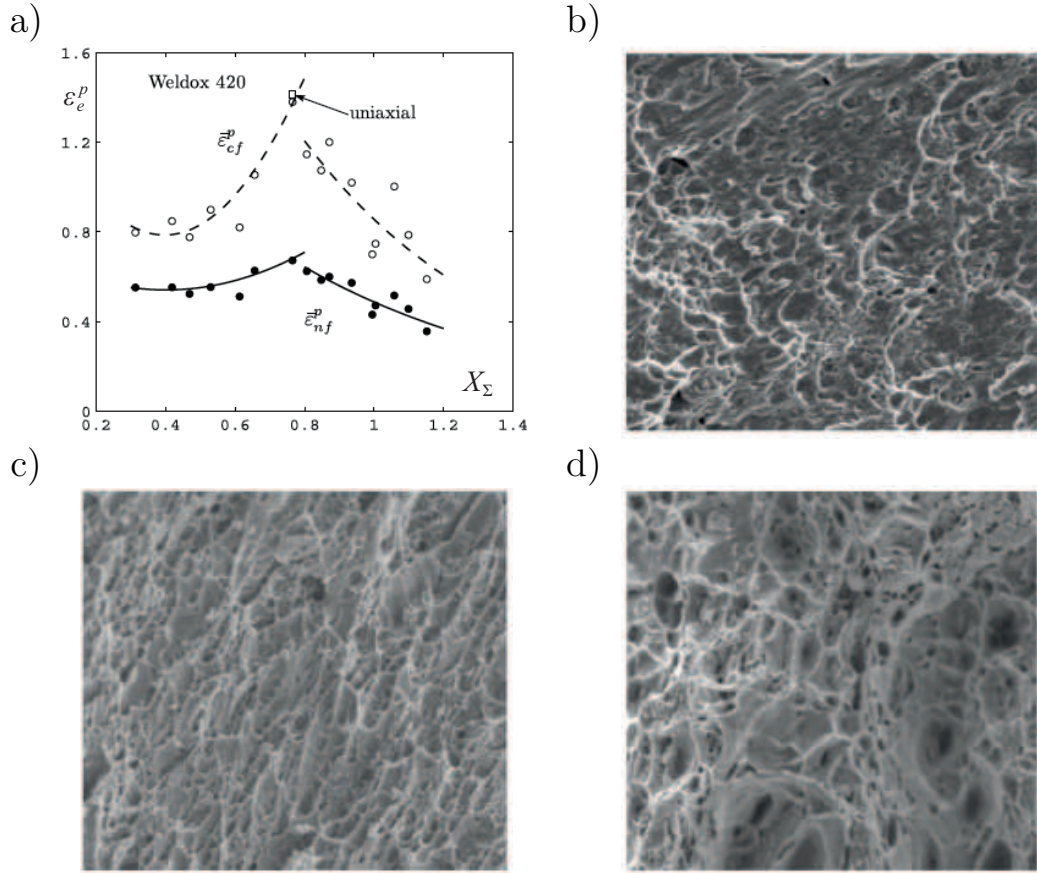


Figure 1: Failure of hot rolled medium-strength steel. (a) Effective plastic strain and failure vs. stress triaxiality. (On the plot, $\bar{\epsilon}_{cf}^p$ and $\bar{\epsilon}_{nf}^p$ refer to the critical plastic strains at the center of a notch and the average plastic strain at the notch, respectively). The rest of the figures correspond to SEM fractographs showing the rupture modes: b) a shear dimple rupture mode with inter-void shearing mechanism and elongated voids for stress triaxiality $X_\Sigma = 0.47$; c) the transition between shear dimples and void growth rupture for $X_\Sigma = 0.85$; d) necking of inter-void ligaments, i.e., void coalescence due to void growth, for $X_\Sigma = 1.10$. All figures are taken from Barsoum and Faleskog (2007a) and correspond to Weldox 420.

91 tion analyses in a self-consistent fashion (Ponte Castañeda and Zaidman, 1994; Kailasam and Ponte Castañeda, 1998).

93 The above-mentioned non-linear homogenization methods have also been extended to include strain hard-
 94 ening elasto-plastic behavior for the matrix material, and implemented numerically in large-scale, structural
 95 finite element programs by Kailasam et al. (2000) and Aravas and Ponte Castañeda (2004). While these
 96 models are quite general, they tend to give overly stiff predictions at high triaxialities (i.e., they are quite
 97 a bit stiffer than the Gurson-based models), especially for small porosity levels. However, this limitation
 98 has been removed, at least for isotropic matrix systems, in recent work by Danas and Ponte Castañeda
 99 (2009a,b), making use of the more accurate “second-order” linear comparison homogenization method of
 100 Ponte Castañeda (2002a,b), and building on earlier works by Danas et al. (2008a), Danas et al. (2008b) and
 101 Danas (2008). The resulting model, which will be referred to here as the SOM model, will be extended to
 102 account for strain-hardening, elasto-plastic behavior for the matrix phase, and will be capable of handling
 103 general “ellipsoidal” particulate microstructures and general three-dimensional loading conditions, including
 104 those leading to pore rotation, while remaining quite accurate at large stress triaxialities and recovering the
 105 Gurson model for purely hydrostatic loadings and spherical pores.

106 Application of the linear comparison constitutive models to various types of loading conditions has
107 revealed the importance of void shape evolution in determining the overall response of plastic porous solids.
108 For example, it was found by [Ponte Castañeda and Zaidman \(1994\)](#) that under uniaxial tension the softening
109 induced by the growth of porosity associated with the Gurson model for ideally plastic porous materials is
110 overpowered by pore shape changes, since the pore elongation in the tensile direction provides a hardening
111 mechanism resulting in overall hardening for the porous material—in agreement with numerical simulations
112 (see [Kailasam et al. \(1997b\)](#)). However, the evolution of the void shape can also induce overall softening of
113 the porous material, and in fact it was shown by [Ponte Castañeda and Zaidman \(1994\)](#), and confirmed by
114 [Danas and Ponte Castañeda \(2009b\)](#), that a porous rigid ideally plastic material could even lose ellipticity
115 by *void collapse* leading to shear band formation at low triaxialities. It is important to emphasize that
116 such an effect could not be captured by the Gurson model, since at low-triaxiality conditions the source
117 of the instability cannot be identified with a void growth mechanism ([Yamamoto, 1978](#)). In this context,
118 it should also be mentioned that [Nahshon and Hutchinson \(2008\)](#) have proposed an *ad hoc* modification of
119 the Gurson model in an attempt to account for softening of the material at low stress triaxialities. While,
120 by construction, this modification brings in an effect of the Lode parameter, it is inconsistent with mass
121 conservation, and still fails to account for the development of morphological anisotropy associated with pore
122 shape changes.

123 Motivated by the above observations, in the present work, we will make use of the SOM model to
124 investigate the influence of the Lode parameter (i.e., the different shear stress states) and the stress triaxiality
125 on the overall behavior of porous elasto-plastic materials and the possible development of “macroscopic”
126 instabilities ([Geymonat et al., 1993](#)) due to the evolution of the underlying microstructure, e.g., void growth
127 and void shape changes. In particular, we will consider two possible failure mechanisms for the porous
128 medium: (i) the existence of a limit load (i.e., a maximum point on the effective stress-strain curve or
129 equivalently zero material hardening rate) and (ii) loss of ellipticity of the incremental response leading to
130 localization of deformation in dilatant shear bands, as discussed originally by [Rice \(1976\)](#). It should be noted
131 in this connection that while loss of ellipticity calculations will lead to predictions that are typically on the
132 high side when compared to experimental results, these are *material* instabilities which can provide useful
133 information about the *theoretical* load-carrying capacity of the material. In actual experiments, the loading
134 conditions and specimen geometry will invariably lead to non-uniform fields, such that the instabilities
135 nucleate at critical locations in the specimen where the local fields are in excess of the applied average fields,
136 leading to progressive failure of the material by propagation of the instability into the specimen.

137 In this work, we will not attempt to model specific experimental conditions, nor structural geometries.
138 However, it is relevant to note that, based on the earlier variational model of [Ponte Castañeda and Zaidman](#)
139 [\(1994\)](#), constitutive user-material subroutines for implementation in finite element codes have been developed
140 by [Kailasam and Ponte Castañeda \(1997\)](#), [Kailasam et al. \(2000\)](#) and [Aravas and Ponte Castañeda \(2004\)](#).
141 Recently, [Danas and Aravas \(in preparation\)](#) have proposed a modification of these earlier models in accord
142 with the present SOM model that recovers the spherical shell solution (i.e., Gurson’s hydrostatic point) at
143 purely hydrostatic loadings, while including all the advanced features of the variational and second-order
144 methods such as arbitrary ellipsoidal void shapes and general loading conditions. In addition, in this work we
145 will not address “microscopic” coalescence criteria (see [Benzerga et al. \(1999\)](#); [Benzerga and Leblond \(2010\)](#)
146 for details on this alternative approach to material failure). It should be remarked in this connection that
147 the incorporation of loss of ellipticity predictions into numerical simulations of actual structural problems
148 (including crack propagation) is a challenging and still largely open problem, which is also beyond the scope
149 of this work.

150 For clarity and simplicity, in our analysis we will consider purely triaxial loading conditions and initially
151 spherical voids so that the void orientation vectors remain aligned with the principal loading conditions
152 for the entire deformation process and therefore do not contribute to the overall material response. Note,
153 however, that for the case of general (non triaxial) loading conditions or initially anisotropic microstruc-
154 tures (i.e., initially ellipsoidal voids misaligned with the laboratory frame axes), the void orientation vec-
155 tors evolve due to finite deformations and could hence affect the overall response of the porous material
156 (e.g., [Kailasam and Ponte Castañeda \(1997\)](#); [Kailasam et al. \(2000\)](#), [Aravas and Ponte Castañeda \(2004\)](#),
157 [Danas and Ponte Castañeda \(2009b\)](#)). The investigation of void rotation effects in this context will be left

158 for future work, but it should be mentioned that recent numerical studies by Barsoum and Faleskog (2007b)
 159 and Tvergaard (2009) have shown that rotation and elongation of the voids along the shearing direction can
 160 contribute to the localization of deformation and subsequent failure of the material.

161 The rest of the paper is organized as follows. First, in section 2, we describe the geometry and loading
 162 conditions, and define the pertinent variables used in this study including the stress triaxiality and the Lode
 163 parameter. In this section, we also describe the microstructure and present a brief summary of the SOM
 164 model, as well as the characterization of the limit load and localization conditions used in this study as failure
 165 criteria for the porous medium. Then, section 3 discusses the results obtained by the SOM for the evolution
 166 of the stress and the underlying microstructure under finite deformations, and compares them with the
 167 (isotropic) modified Gurson model of Nahshon and Hutchinson (2008), referred to as MGUR below. Limit
 168 load and localization maps are constructed as a function of the stress triaxiality and the Lode parameter.
 169 A parametric study to investigate the influence of the material hardening rate and initial porosity on the
 170 limit load and localization maps is also carried out. Finally, we conclude with some general comments and
 171 perspectives for future work.

172 2. The non-linear homogenization model

173 This section briefly describes the application of the “second-order” nonlinear homogenization model
 174 (SOM) of Danas and Ponte Castañeda (2009a) for porous elasto-plastic materials subjected to triaxial load-
 175 ing conditions. We first define the stress triaxiality and Lode parameters, followed by microstructural
 176 variables describing the volume fraction, shape, distribution and orientation of the voids. Next, building on
 177 the work of Aravas and Ponte Castañeda (2004), we develop consistent constitutive relations for the elastic
 178 and plastic deformations of the porous medium, and provide evolution laws for the above-mentioned mi-
 179 crostructural variables, as well as the strain hardening law for the matrix material. Finally, expressions for
 180 the hardening rate and the localization conditions are derived.

181 2.1. Triaxial loading conditions: Stress triaxiality and Lode parameter

182 This subsection discusses the loading conditions and the associated stress measures used to distinguish
 183 between hydrostatic loading and different shear stress states. We consider purely triaxial loading conditions
 184 with the principal stresses $\sigma_1 = \sigma_{11}$, $\sigma_2 = \sigma_{22}$ and $\sigma_3 = \sigma_{33}$ ($\sigma_{ij} = 0$ for $i \neq j$) being aligned with the
 185 laboratory frame axes, $\mathbf{e}^{(1)}$, $\mathbf{e}^{(2)}$ and $\mathbf{e}^{(3)}$, respectively. This allows for the definition of alternative stress
 186 measures that are more appropriate for dilatational plasticity of porous materials. The three alternative
 187 measures are the hydrostatic (or mean) stress, σ_m , the von Mises equivalent (or effective) stress, σ_e , and
 188 the third invariant of the stress deviator, J_3 , defined as

$$189 \quad \sigma_m = \sigma_{kk}/3, \quad \sigma_e = \sqrt{3 J_2} = \sqrt{3 s_{ij} s_{ij}/2}, \quad J_3 = \det(s_{ij}), \quad (1)$$

190 where $s_{ij} = \sigma_{ij} - \sigma_m \delta_{ij}$ is the stress deviator. Using these definitions, we can readily define the stress
 191 triaxiality, X_Σ , and Lode angle, θ , or Lode parameter¹, L , via the following expressions

$$192 \quad X_\Sigma = \frac{\sigma_m}{\sigma_e}, \quad L = -\cos 3\theta = -\frac{27 J_3}{2 \sigma_e^3}. \quad (2)$$

193 By definition, the range of values for the X_Σ and L , (or θ) are

$$194 \quad -\infty < X_\Sigma < \infty, \quad \text{and} \quad -1 \leq L \leq 1 \quad \text{or} \quad 0 \leq \theta \leq \pi/3. \quad (3)$$

195 Then, relations (2) can be used to express the principal stresses as functions of X_Σ , σ_e and θ , such that

$$196 \quad \frac{3}{2\sigma_e} \{\sigma_1, \sigma_2, \sigma_3\} = \left\{ -\cos\left(\theta + \frac{\pi}{3}\right), -\cos\left(\theta - \frac{\pi}{3}\right), \cos\theta \right\} + \frac{3}{2} X_\Sigma \{1, 1, 1\}. \quad (4)$$

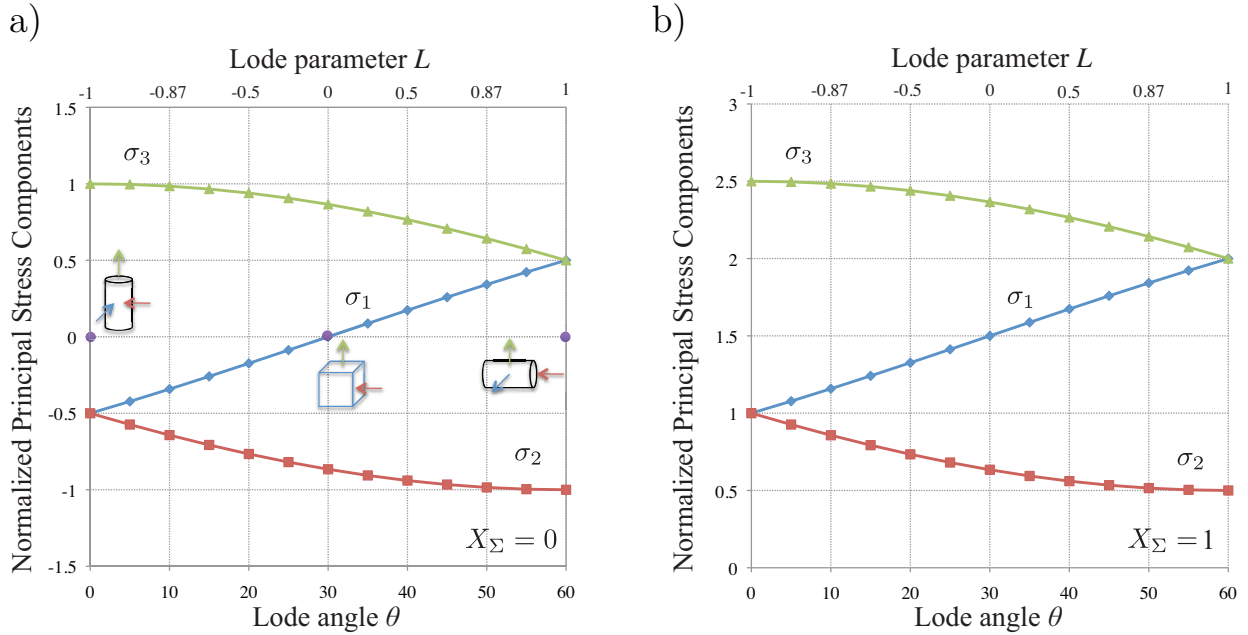


Figure 2: Normalized principal stresses $\frac{3}{2\sigma_e}\{\sigma_1, \sigma_2, \sigma_3\}$, as a function of the Lode angle θ or equivalently the Lode parameter L . Parts (a) and (b) correspond to stress triaxialities $X_\Sigma = 0$ and $X_\Sigma = 1$, respectively.

197 Fig. 2 shows the normalized principal stresses defined in (4) as a function of the Lode parameter L and
 198 Lode angle θ for (a) $X_\Sigma = 0$ and (b) $X_\Sigma = 1$. It is clear from Fig. 2a that for $L = -1$ or $\theta = 0$, the stress
 199 state is axisymmetric with one positive and two negative stresses (axisymmetric tension). On the other
 200 end, when $L = 1$ or $\theta = \pi/3$, the stress state is also axisymmetric but with two positive and one negative
 201 stresses (biaxial tension with axisymmetric compression). Note that these two different axisymmetric states
 202 lead to different evolution of the underlying microstructure and therefore to different overall responses as
 203 the deformation progresses. When, $L = 0$ or $\theta = \pi/6$, the stress state is in-plane shear with one stress
 204 identically equal to zero (e.g., plane stress state). The rest of the states are between axisymmetric and
 205 in-plane shear states. It should be noted that when the stress triaxiality is nonzero then the principal
 206 stresses are simply translated by a constant either upwards for $X_\Sigma > 0$, as shown in Fig. 2b for $X_\Sigma = 1$, or
 207 downwards for $X_\Sigma < 0$ (not shown here for brevity). Note also that $|X_\Sigma| \rightarrow \infty$ and $X_\Sigma = 0$ correspond to
 208 purely hydrostatic and purely deviatoric loadings, respectively.

209 2.2. Microstructure

210 The porous material is composed of two phases. The matrix phase is elasto-plastic and isotropic fol-
 211 lowing a J_2 flow rule with isotropic strain hardening described by the yield stress σ_y as a function of the
 212 accumulated equivalent plastic strain ε_M^p . The inclusion phase is vacuous and consists of initially spherical
 213 voids distributed uniformly and isotropically, such that the initial response of the porous medium is also
 214 isotropic. However, due to the finite deformations considered in this problem the voids evolve into non-
 215 spherical shapes and hence the porous medium becomes locally anisotropic (i.e., develops morphological
 216 anisotropy). Consequently, it is necessary to define microstructural variables that not only describe the
 217 volume fraction of the voids, as is the case in the models of Gurson (1977) and Nahshon and Hutchinson
 218 (2008), but also their shape, distribution and orientation.

¹Note that our choice for the Lode parameter L differs from the standard definition, $\mu = (2\sigma_1 - \sigma_3 - \sigma_2)/(\sigma_3 - \sigma_2)$, but the two parameters are simply related by $L = \mu(9 - \mu^2)/\sqrt{(\mu^2 + 3)^3}$, and therefore agree for the values $-1, 0$, and $+1$.

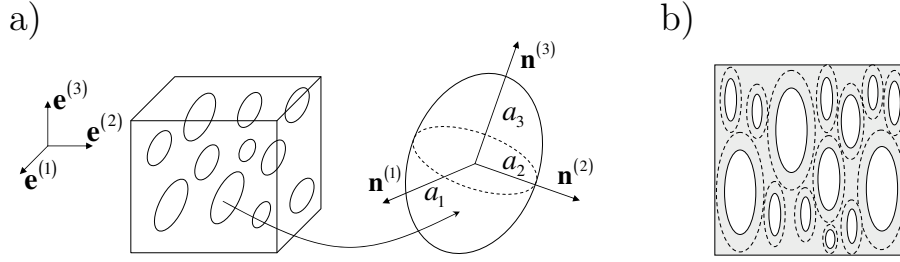


Figure 3: Graphical representation of the microstructure. Part (a) shows the local orientation axes $\mathbf{n}^{(i)}$ with $i = 1, 2, 3$ of a representative ellipsoidal void with semi-axis a_1 , a_2 and a_3 . Part (b) shows the a cross-section of the specimen where the “white” ellipsoids denote voids with ellipsoidal shape while the dashed ellipsoids refer to the distribution of their centers.

219 According to the schematic representation shown in Fig. 3a and at some finite deformation state, we
 220 consider that the porous material is characterized by a “particulate” microstructure consisting of *ellipsoidal*
 221 voids (i.e., with semi-axes $a_1 \neq a_2 \neq a_3$) aligned in a certain direction as a result of the previously described
 222 triaxial loading conditions. In addition, it is assumed (Willis, 1978; Ponte Castañeda and Willis, 1995)
 223 that the centers of the voids are distributed with *ellipsoidal* symmetry (see Fig. 3b). This description
 224 of a particulate microstructure represents a generalization of the Eshelby (1957) dilute microstructure to
 225 the non-dilute regime. In this work, which is based on the model of Danas and Ponte Castañeda (2009a),
 226 we will make the simplifying assumption that the ellipsoidal shape and orientation of the distribution
 227 function is *identical* to the ellipsoidal shape and orientation of the voids at each stage of the deformation.
 228 This is schematically shown in Fig. 3b, where the dashed ellipsoids representing the pore distribution
 229 are taken to have the same ellipsoidal shape as the actual pores (in white). This assumption has been
 230 shown (Danas and Ponte Castañeda, 2009b) to provide accurate estimates, especially at small to moderate
 231 porosities. Nonetheless, it should be mentioned that, in general, the void distribution shape could be different
 232 from the void shape, as discussed by Ponte Castañeda and Willis (1995), and this effect can be accounted
 233 for at least approximately (Kailasam et al., 1997a).

234 Moreover, in the present study we consider purely triaxial loading conditions and initially isotropic
 235 materials (i.e., comprising initially spherical voids). This implies that the orientation of the voids remains
 236 fixed and aligned with the triaxial loading conditions. Thus, the vectors $\mathbf{n}^{(i)}$ (with $i = 1, 2, 3$) denoting the
 237 orientation of the principal axes of the voids (see Fig. 3a) remain aligned with the principal laboratory axes
 238 $\mathbf{e}^{(i)}$. Consequently, the porous medium becomes, at most, orthotropic with finite deformations, with the
 239 axes of orthotropy coinciding with the principal axes of the ellipsoidal voids and the laboratory frame axes,
 240 i.e., with $\mathbf{n}^{(i)} = \mathbf{e}^{(i)}$. It should be emphasized, however, that the model of Danas and Ponte Castañeda
 241 (2009a) can account for more general loading conditions, non-spherical initial void shapes and rotation of
 242 voids, as has already been shown in Danas (2008) and Danas and Ponte Castañeda (2009b), but such a
 243 study is not carried out here because it will not be needed to describe the effects of interest in this work.

244 In view of the above hypotheses, the relevant internal variables describing the state of the microstructure
 245 in this problem are:

$$s_\alpha = \{\varepsilon_M^p, f, w_1, w_2\}, \quad (5)$$

247 where ε_M^p is the accumulated plastic strain in the undamaged matrix phase, f is the porosity (i.e., volume
 248 fraction of the voids), and $w_1 = a_3/a_1$ and $w_2 = a_3/a_2$ are two aspect ratios characterizing the ellipsoidal
 249 shape of the voids (with a_1 , a_2 and a_3 denoting the principal semi-axes of the ellipsoidal voids) and their
 250 distribution function.

251 2.3. Elasto-plastic constitutive relations

252 The overall strain-rate \mathbf{D} in the porous material is decomposed into its elastic and plastic parts via

$$\mathbf{D} = \mathbf{D}^e + \mathbf{D}^p, \quad (6)$$

254 where \mathbf{D}^e and \mathbf{D}^p , respectively, denote the elastic and plastic parts. Note that due to the presence of voids
 255 the overall material behavior is compressible (i.e., pressure dependent) implying that the plastic strain-rate
 256 tensor is not deviatoric (i.e., $\mathbf{D}_{kk}^p \neq 0$). On the other hand, due to the triaxial loading conditions and the fact
 257 that the voids do not rotate during the deformation process, the overall spin as well as the microstructural
 258 spins are identically zero. In addition, in view of the fact that the pores can carry no loads and following
 259 [Aravas and Ponte Castañeda \(2004\)](#), it is assumed that the elastic and plastic parts of the strain rate can
 260 be estimated by independent, but consistent homogenization analyses.

261 Thus, the elastic response of the porous material is described in terms of an effective compliance tensor
 262 \mathbf{M} via

$$263 \quad D_{kl}^e = M_{ijkl} \dot{\sigma}_{ij}, \quad \text{with} \quad M_{ijkl} = M_{ijkl}^M + \frac{f}{1-f} Q_{ijkl}^{-1}, \quad (7)$$

264 where $\dot{\sigma}$ represents the material time derivative of the stress, which will be taken here to be given by the
 265 (partial) derivative with respect to time, since the stress is assumed to be uniform and the spin is zero,
 266 and $\mathbf{Q} = \mathbf{Q}(w_1, w_2, \mathbf{n}^{(i)} = \mathbf{e}^{(i)})$ is directly related to the well-known Hill or Eshelby tensor for ellipsoidal
 267 microstructures and its evaluation is detailed in [Willis \(1981\)](#) (see also [Danas \(2008\)](#)). The fourth-order
 268 tensor \mathbf{M}^M is the compliance modulus of the matrix (metallic) phase and is taken to be isotropic such that

$$269 \quad M_{ijkl}^M = \frac{1+\nu}{E} \left[\frac{1}{2} (\delta_{ik} \delta_{jl} + \delta_{il} \delta_{jk}) - \frac{\nu}{1+\nu} \delta_{ij} \delta_{kl} \right], \quad (8)$$

270 where E and ν denote the elastic modulus and Poisson ratio, respectively.

271 On the other hand, the yield condition for the porous material can be written in the functional form

$$272 \quad \Phi(\boldsymbol{\sigma}; s_\alpha) = \hat{\sigma}_{eq}(\boldsymbol{\sigma}; f, w_1, w_2) - \sigma_y(\varepsilon_M^p) = 0, \quad (9)$$

273 where $\hat{\sigma}_{eq}$ is a scalar function of the stress tensor and the microstructural variables, which is detailed in
 274 [Danas and Ponte Castañeda \(2009a\)](#) (*c.f.* equations (25) and (28)), while σ_y is the effective stress governing
 275 flow of the undamaged matrix material and in general depends on the accumulated plastic strain ε_M^p in the
 276 matrix phase. The overall plastic strain rate \mathbf{D}^p of the porous material is then obtained from the normality
 277 rule via

$$278 \quad D_{ij}^p = \dot{\Lambda} N_{ij}, \quad N_{ij} = \frac{\partial \Phi}{\partial \sigma_{ij}}, \quad (10)$$

279 where $\dot{\Lambda} \geq 0$ is the plastic multiplier, which is determined by the consistency condition as discussed in subsec-
 280 tion 2.5, and N_{ij} is the normal to the yield surface Φ . The reader is referred to [Danas and Ponte Castañeda](#)
 281 [\(2009a\)](#) for more detailed expressions for Φ and N_{ij} .

282 2.4. Evolution equations

283 Following the work of [Ponte Castañeda and Zaidman \(1994\)](#), [Kailasam and Ponte Castañeda \(1998\)](#),
 284 [Aravas and Ponte Castañeda \(2004\)](#) and [Danas and Ponte Castañeda \(2009a\)](#), evolution equations are given
 285 in this section for the microstructural variables ε_M^p , f , w_1 and w_2 defined in relation (5). Once again, in this
 286 work the orientation vectors remain aligned with the principal loading directions, i.e., $\mathbf{n}^{(i)} = \mathbf{e}^{(i)}$ ($i = 1, 2, 3$),
 287 during the deformation process.

288 The evolution equation for the accumulated plastic strain in the matrix phase ε_M^p is determined by the
 289 condition ([Gurson, 1977](#)) that the macroscopic plastic work $\sigma_{ij} D_{ij}^p$ be equal to the corresponding microscopic
 290 plastic work $(1-f) \sigma_y \dot{\varepsilon}_M^p$, which implies that

$$291 \quad \dot{\varepsilon}_M^p = \frac{\sigma_{ij} D_{ij}^p}{(1-f) \sigma_y} = \dot{\Lambda} \frac{\sigma_{ij} N_{ij}}{(1-f) \sigma_y}. \quad (11)$$

292 For strain hardening materials, σ_y is a function of ε_M^p , which, in general, is to be extracted from experimental
 293 uniaxial stress-strain curves. In our work, a rather general strain hardening law for $\sigma_y(\varepsilon_M^p)$ will be given in
 294 the results section.

295 Any changes of the pores are assumed to be only the result of plastic deformations (Aravas and Ponte Castañeda,
 296 2004) while elastic deformations are considered to have a negligible effect on the evolution of the voids volume
 297 fraction. Noting further that the matrix material is plastically incompressible (J_2 plasticity), the evolution
 298 equation for the porosity f follows easily from the continuity equation and reads

$$299 \quad \dot{f} = (1 - f) D_{kk}^p = \dot{\Lambda} (1 - f) \frac{\partial \Phi}{\partial \sigma_{kk}}. \quad (12)$$

300 We point out that void nucleation is not considered in the above relation but can be readily included
 301 by proper modification of (12) (e.g., Needleman and Rice (1978); Chu and Needleman (1980); Tvergaard
 302 (1990)).

303 The evolution of the aspect ratios w_1 and w_2 , describing the shape of the voids, is given in terms of the
 304 average strain-rate in the vacuous phase \mathbf{D}^v such that

$$305 \quad \dot{w}_s = w_s (n_i^{(3)} n_j^{(3)} - n_i^{(s)} n_j^{(s)}) D_{ij}^v = \dot{\Lambda} y_w^{(s)} (\boldsymbol{\sigma} / \sigma_y; s_\alpha), \quad \text{with } \mathbf{n}^{(i)} = \mathbf{e}^{(i)}, \quad (13)$$

306 and no sum on $s = 1, 2$. The average strain-rate \mathbf{D}^v in the vacuous phase is estimated via the linear
 307 comparison material, as discussed in Danas and Ponte Castañeda (2009a) (see equation (76) in that refer-
 308 ence). Finally, the associated functions $y_w^{(s)}$ have also been given in Danas and Ponte Castañeda (2009a)
 309 (see relation (80) in that reference) and will not be repeated here.

310 2.5. The consistency condition and the hardening rate

311 In this subsection, we determine the plastic multiplier $\dot{\Lambda}$ and hardening rate H by means of the consistency
 312 condition (Dafalias, 1985) for continuously applied loading, which in this case reads

$$313 \quad \dot{\Phi} = \frac{\partial \Phi}{\partial \sigma_{kl}} \dot{\sigma}_{kl} + \frac{\partial \Phi}{\partial \varepsilon_M^p} \dot{\varepsilon}_M^p + \frac{\partial \Phi}{\partial f} \dot{f} + \sum_{s=1,2} \frac{\partial \Phi}{\partial w_s} \dot{w}_s = 0. \quad (14)$$

314 Substitution of the evolution equations (11), (12), (13), and of $\partial \Phi / \partial \varepsilon_M^p = -d\sigma_y / d\varepsilon_M^p$, in this last relation
 315 provides the following expression for the plastic multiplier

$$316 \quad \dot{\Lambda} = \frac{1}{H} \frac{\partial \Phi}{\partial \sigma_{kl}} \dot{\sigma}_{kl} = \frac{1}{H} N_{kl} \dot{\sigma}_{kl}, \quad (15)$$

317 where H is the hardening rate defined by

$$318 \quad H = \frac{\sigma_{ij} N_{ij}}{(1 - f) \sigma_y} \frac{d\sigma_y}{d\varepsilon_M^p} - (1 - f) N_{kk} \frac{\partial \Phi}{\partial f} - \sum_{s=1,2} \frac{\partial \Phi}{\partial w_s} y_w^{(s)}. \quad (16)$$

319 The hardening rate is a measure of the overall hardening of the porous material. When $H > 0$, the material
 320 is said to harden, while when $H < 0$, it is said to soften. The critical point when $H = 0$ usually provides
 321 the transition from the hardening regime to the softening regime, and can be identified with the maximum
 322 stress or limit load of the material. Clearly, the maximum stress is important for stress-controlled boundary
 323 conditions, since the material will not be able to support stresses exceeding the limit load, and the material
 324 will fail at this point under increasing stress.

325 By observation of relation (16), we note that the first two terms of the right-hand side appear also in the
 326 Gurson (1977) and the Nahshon and Hutchinson (2008) models, and incorporate the effects of the matrix
 327 strain hardening and the evolving porosity (or damage in Nahshon and Hutchinson (2008)) on the overall
 328 response of the porous material. By contrast, in the present model, additional terms appear in (16), due to
 329 void shape changes. This last term of the right hand side in (16), which comprises the evolution of the two
 330 aspect ratios w_1 and w_2 , affects the overall hardening rate of the porous material in a nontrivial manner.
 331 All these effects will be investigated in detail in the next section.

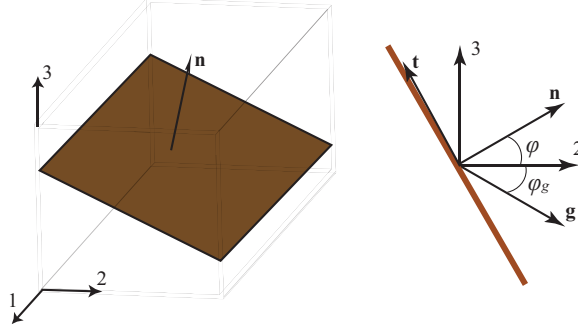


Figure 4: Graphical representation of a localization band. The figure on the right shows the local system of coordinates, where \mathbf{n} is the normal to the band and \mathbf{t} is the tangent. The angle between \mathbf{n} and \mathbf{g} provides the deformation inside the band. For instance, if $\mathbf{n} \perp \mathbf{g}$, the deformations inside the band is a simple shear. However, due to the compressibility of the porous material \mathbf{g} is not, in general, perpendicular to \mathbf{n} and the deformation inside the band can also have normal components (e.g., $n_i D_{ij} n_j \neq 0$), leading to the formation of a dilatant shear band.

332 2.6. Localization conditions

333 In this subsection, we summarize the localization conditions corresponding to the loss of ellipticity of the
 334 governing equations and leading to non-unique solutions, bifurcations and instabilities, as described by Rice
 335 (1976). By making use of definition (15), the incremental constitutive relations (6), (7) and (10) describing
 336 the overall elasto-plastic response of the porous material can be written in the form

$$337 \quad \dot{\sigma}_{ij} = L_{ijkl}^{inc} D_{kl}, \quad \text{where} \quad L_{ijkl}^{inc} = L_{ijkl} - \frac{N_{pq} L_{pqij} L_{klmn} N_{mn}}{H + N_{rs} L_{rsuv} N_{uv}} \quad (17)$$

338 is the effective incremental elasto-plastic modulus of the porous material, and $\mathbf{L} = \mathbf{M}^{-1}$ is the effective
 339 elastic modulus of the porous material.

340 Following Rice (1976), we consider an infinite porous medium with no initial imperfections, which implies
 341 that the trivial solution to this problem is homogenous deformation throughout the infinite region. Then,
 342 we look for conditions under which the deformation would localize inside a thin band leading to unloading
 343 outside the band, as shown schematically in Fig. 4. This second solution to the problem is a discontinuous
 344 bifurcation of the uniform solution and leads to a lower energy state than the uniform one. As already known,
 345 the specimen would tend to localize earlier if an initial imperfection were considered. However, the goal
 346 of the present study is to investigate pure material instabilities leaving aside any geometrical imperfections
 347 for a future study where actual boundary value problems resulting from experimental geometries will be
 348 investigated.

349 In any event, the condition for the localization of deformation inside a thin band with normal n_i becomes
 350 (Rice, 1976; Needleman and Rice, 1978)

$$351 \quad \det [n_i L_{ijkl}^{inc} n_l + A_{jk}] = 0, \quad \text{where} \quad 2A_{jk} = -\sigma_{jk} + \sigma_{js} n_s n_k + (n_p \sigma_{pq} n_q) \delta_{jk} - n_j n_r \sigma_{rk}. \quad (18)$$

352 When this localization condition is first met in a program of deformation, the difference between the total
 353 strain-rate inside and outside the band can be written as $\Delta D_{ij} = (g_i n_j + n_i g_j)/2$, with g_i being a function
 354 only of distance across the localization band $n_i x_i$ (with x_i being the position vector). The use of n_i and
 355 g_i provide information about the deformation state inside the localization band. For instance, in the case
 356 that the material is fully incompressible, it can be shown that g_i is perpendicular to n_i and parallel to the
 357 band tangent vector t_i which implies that the deformation state in the band is simple shear, i.e., a shear
 358 localization band. In the present study, however, the material is compressible due to the finite porosity,
 359 and can accommodate deformation states other than simple shear inside the band. In that case, n_i and
 360 g_i are not necessarily perpendicular to each other as shown in Fig. 4, which can lead to a nonzero normal
 361 component of the deformation state inside the band, i.e., $n_i \Delta D_{ij} n_j \neq 0$.

362 In connection with the above-described localization conditions, it should be emphasized that the (uni-
363 form) solutions obtained directly from the constitutive model for the porous material would cease to be
364 valid at the point of the instability. Then, a post-bifurcation analysis would be required beyond this point.
365 Such an analysis should make use of geometrical effects or initial imperfections and is outside the scope of
366 the present work, which focuses on uniform solutions under fixed stress triaxialities and Lode parameter
367 loadings throughout the entire deformation history. However, in the results to be described in the next
368 section, the (uniform) solutions will still be shown beyond the onset of said instabilities, mostly because
369 they are suggestive of the mode of the onset of the instability. Of course, such solutions are not meant to be
370 representative of what actually happens beyond the instability. As already known from investigation in other
371 contexts (e.g., failure of fiber-reinforced composites), the final failure mode requires the full post-bifurcation
372 analysis. More often than not, such failure modes are inherently different from the mode of the onset of the
373 instability.

374 3. Results and discussion

375 As already mentioned in the previous section, our objective is to investigate the effects of the stress
376 triaxiality X_Σ and Lode parameter L (or Lode angle θ) on the macroscopic response and failure of porous
377 elasto-plastic materials subjected to triaxial loading conditions. Given the fact that a maximum stress is ex-
378 pected, in this work the strain rate D_{33} will be prescribed, together with the values of X_Σ and L , which will
379 serve to determine all three (principal) stresses, σ_1 , σ_2 and σ_3 , as well as the evolution of the microstructural
380 variables, the porosity f , and the average aspect ratios, w_1 and w_2 , as functions of time t . However, it will be
381 convenient to use as a time-like variable the total equivalent strain $\varepsilon_e = \int_t \sqrt{2D'_{ij}D'_{ij}/3} dt$, with D'_{ij} denoting
382 the strain-rate deviator, and to consider the overall von Mises equivalent stress σ_e instead of the individual
383 stress components in the characterization of the macroscopic response. Because of the special loading con-
384 ditions imposed, it can be shown that the maximum on the σ_e versus ε_e plots will correspond exactly to a
385 vanishing hardening rate $H = 0$, indicating a possible instability under stress-controlled loading conditions.
386 In addition, the loss of ellipticity condition will be determined for the material making use of the condi-
387 tion (18). For completeness, a comparison will also be made between the predictions of the “second-order”
388 model (SOM) of [Danas and Ponte Castañeda \(2009a\)](#) and the modified Gurson model (MGUR) proposed
389 by [Nahshon and Hutchinson \(2008\)](#). In keeping with standard practice ([Barsoum and Faleskog, 2007a](#)), the
390 maximum stress (i.e., the locus of points where $H = 0$) and loss of ellipticity (LOE) conditions will be dis-
391 played in terms of the total equivalent plastic strain (or effective plastic strain) $\varepsilon_e^p = \int_t \sqrt{2(D_{ij}^p)'(D_{ij}^p)'/3} dt$,
392 with $(D_{ij}^p)'$ denoting the plastic strain-rate deviator. In this work, the resistance of the material to failure
393 by either condition will be referred to as the overall ductility. Furthermore, it should be emphasized, that as
394 a consequence of the very small magnitude of the overall elastic strains, the difference between the overall
395 total strain and the overall plastic strain is very small for all practical purposes. Finally, a parametric study
396 will be carried out to investigate the influence of different matrix strain hardening exponents and initial
397 porosities on the limit load and LOE maps.

398 3.1. Material parameters and initial conditions

399 The Young’s modulus and Poisson’s ratio of the matrix phase are taken to be $E = 200\text{GPa}$ and $\nu = 0.3$,
400 respectively, and the matrix phase to exhibit isotropic strain hardening following the law²

$$401 \quad \sigma_y(\varepsilon_M^p) = \sigma_0 \left(1 + \frac{\varepsilon_M^p}{\varepsilon_0} \right)^N, \quad \varepsilon_0 = \sigma_0/E. \quad (19)$$

²It should be noted here that any hardening law for the matrix phase involving temperature effects or different non-monotonic strain hardening stages can be readily taken into account. However, the simple isotropic model will suffice for the purposes of this work.

402 In this expression, σ_0 and ε_0 denote the initial yield stress and yield strain of the matrix material (i.e., the
 403 material with $f = 0$), and $N \leq 1$ is the strain hardening exponent. Typical values for these parameters
 404 are $\sigma_0 = 200\text{MPa}$ and $N = 0.1$, which will be used throughout this work except in section 3.4 where a
 405 parametric study is carried out with $N = 0.01, 0.05, 0.1$ and 0.2 .

406 The matrix phase is taken to be initially unloaded with zero accumulated plastic strain $\varepsilon_M^p = 0$, while
 407 the voids are initially spherical with $w_1 = w_2 = 1$. The initial porosity is taken to be $f_0 = 1\%$ except in
 408 section 3.4 where a parametric study is carried out with $f_0 = 0.1\%, 1\%$ and 5% . It should be noted that
 409 the dependence of the failure maps on the Young’s modulus, and Poisson’s ratio has been found to be weak,
 410 and for this reason no results will be reported here for different values of these parameters.

411 3.2. Stress-strain response and microstructure evolution results

412 In order to investigate the main effects of the stress triaxiality and Lode parameter on the effective
 413 response of the porous material, we show results for three representative values of stress triaxialities, $X_\Sigma =$
 414 $0.1, 0.6, 1$, and four of the Lode parameter, $L = -1, -0.5, 0, 1$ (or Lode angle $\theta = 0, 20, 30, 60^\circ$, respectively).

415 Fig. 5 shows plots of (a) the equivalent stress σ_e , (b) the porosity f , and the aspect ratios (c) w_1 and (d)
 416 w_2 , as a function of the equivalent strain ε_e , for given values of the Lode parameter and a *low* value of the
 417 stress triaxiality ($X_\Sigma = 0.1$). The main observation in Fig. 5a is that the Lode parameter strongly affects
 418 the onset of softening (i.e., maximum load) and localization of the porous material. For axisymmetric tensile
 419 loadings ($L = -1$), the stress increases following the prescribed strain hardening law of the matrix phase
 420 ($N = 0.1$ here). On the other hand, for $L = -0.5, 0$, and 1 , we observe abrupt drops in σ_e at different levels
 421 of the total strain ε_e , indicating a sudden loss in the load-carrying capacity of the material. In addition, after
 422 the maximum stress σ_e (see inset graph in Fig. 5a) or limit load (black dot on the graph) strong softening
 423 of the material is observed eventually leading to localization and hence loss of ellipticity (open circle on the
 424 graph) of the homogenized equations.

425 With the objective of shedding light on the mechanism leading to this sharp stress drop, it is necessary
 426 to consider the evolution of the microstructural variables, f , w_1 and w_2 , provided in Figs. 5 (b), (c) and
 427 (d), respectively. In part (b), we observe an overall reduction in the porosity f as a function of ε_e up to the
 428 point of the limit load (black dot on the graph), followed by a sharp increase in f shortly after the maximum
 429 stress has been achieved. It is clear by Fig. 5b that at the strain level at which the limit load and loss of
 430 ellipticity occur, the porosity is still very small. Therefore, the corresponding stress drop observed in part
 431 (a) cannot be due to the increase in the porosity, and the only microstructural variables that can possibly
 432 affect the overall response of the porous material are the aspect ratios, w_1 and w_2 . As shown in part (c), w_1
 433 can become rather large for $L = -1$, but remains below the value of 5 for $L > -0.5$. On the other hand, as
 434 shown in part (d), w_2 increases very fast for all values of $L > -1$. In particular, for $L = 1$ (corresponding
 435 to axisymmetric compression along the x_2 direction, see Fig. 2a), $w_1 = 1$, while w_2 blows up at a certain
 436 “critical” value of ε_e (around 0.6). This means that the voids *collapse* in the x_2 direction, becoming flattened
 437 cracks (lying in the $x_1 - x_3$ plane) with $a_2 \rightarrow 0$, while the material becomes locally anisotropic (i.e., exhibits
 438 morphological anisotropy due to the very significant void shape changes). However, since the porosity f
 439 remains finite at this “critical” point where $a_2 \rightarrow 0$, $a_1 = a_3$ must tend to infinity, suggesting coalescence of
 440 the voids in the $x_1 - x_3$ plane.

441 To clarify this failure mechanism further, it is recalled here that the aspect ratios serve to denote both
 442 the shape of the voids as well as the shape of their distribution function. Hence, as $a_2 \rightarrow 0$ and $a_1 = a_3 \rightarrow \infty$
 443 both the shape of the voids and the shape of their distribution function become extremely flat in the $x_1 - x_3$
 444 plane. This observation together with the fact that the porosity is small but finite, implies that the pores
 445 grow without a bound in the $x_1 - x_3$ plane, eventually linking up to form “layers” of pores in the solid
 446 material, which can be associated with void coalescence in that plane and subsequent loss of the load-
 447 carrying capacity of the material in the transverse direction. Such a failure mechanism would be consistent
 448 with the “flat” dimples observed in Fig. 1b from the experimental results of Barsoum and Faleskog (2007a)
 449 at low stress triaxialities. (Note, however, that the presence of the second-phase particles may interfere with
 450 the collapse of the voids, and should be accounted for in situations where the voids are not pre-existing, but
 451 instead nucleate from second-phase particles.) For other values of L with $-1 < L < 1$, essentially the same
 452 mechanism is observed except that in this case the pores also change shape in the collapse plane ($x_1 - x_3$).

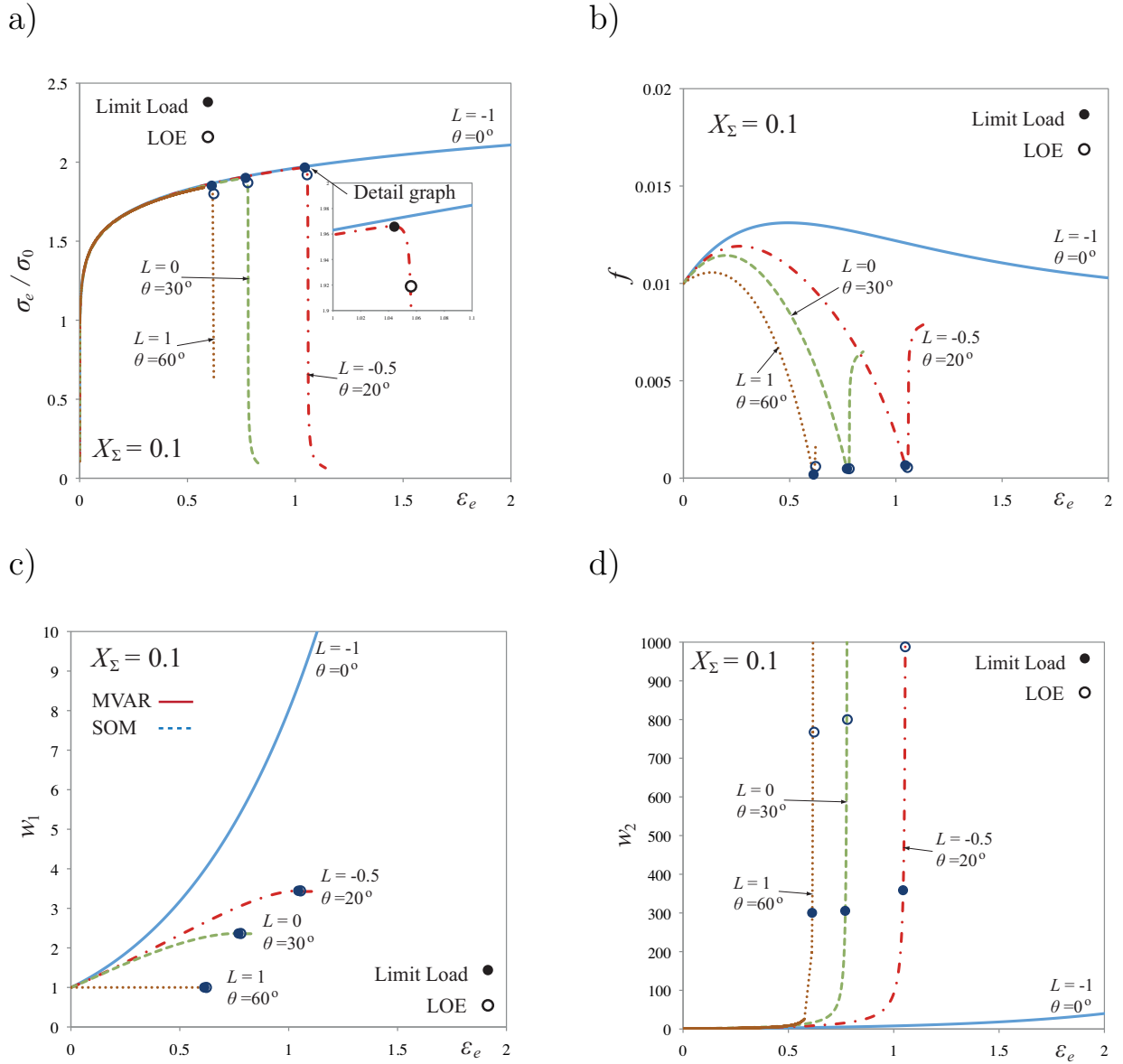


Figure 5: Plots of the SOM estimates for (a) the equivalent stress σ_e , (b) the porosity f , and the aspect ratios (c) w_1 and (d) w_2 as a function of the equivalent strain ε_e , for a low value of the stress triaxiality ($X_\Sigma = 0.1$) and four values of the Lode parameter. The influence of the Lode parameter is dramatic at low triaxialities mainly due to the extremely sharp evolution of the aspect ratio w_2 in (d). The strain hardening exponent is $N = 0.1$ and the initial porosity $f_0 = 1\%$. The inset in part (a) shows a blow up of the region around the maximum stress for $L = -0.5$ (or $\theta = 20^\circ$).

453 However, as can be seen in Figs. 5a and d, the effect becomes more pronounced as the value of L increases
 454 from -1 toward $+1$. At the extreme value of $L = -1$, the shape of the pores is constrained to remain
 455 circular in the $x_1 - x_2$ cross-section, and this kinematic restriction prevents collapse of the pores, explaining
 456 the lack of a maximum stress point and corresponding loss of ellipticity in this case.

457 Fig. 6 shows plots of σ_e , f , w_1 and w_2 as a function of the equivalent strain ε_e , for several fixed values
 458 of the Lode parameter L and for a *high* value of the stress triaxiality ($X_\Sigma = 1$). The main result is that

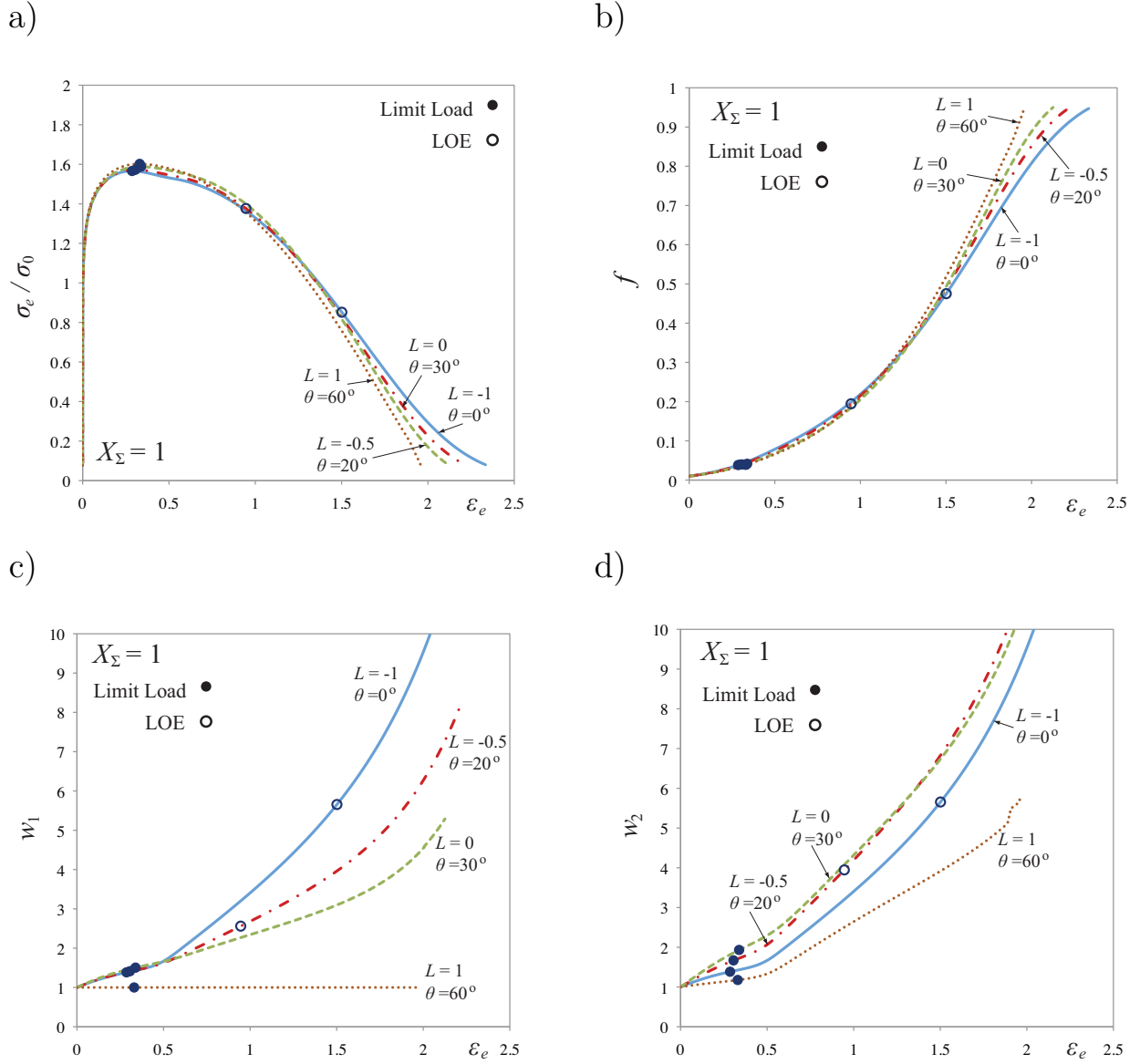


Figure 6: Plots of the SOM estimates for (a) the equivalent stress σ_e , (b) the porosity f , and the aspect ratios (c) w_1 and (d) w_2 as a function of the equivalent strain ε_e , for a high value of the stress triaxiality ($X_\Sigma = 1$) and four values of the Lode parameter. The influence of the Lode parameter becomes negligible in this case since the response of the porous material is dominated by the significant evolution of porosity f . The strain hardening exponent is $N = 0.1$ and the initial porosity $f_0 = 1\%$.

459 the effect of the Lode parameter on the overall mechanical response of the porous material is negligible, as
 460 can be seen in Fig. 6a, since all the $\sigma_e - \varepsilon_e$ curves almost coincide. In particular, they exhibit a limit load
 461 at rather low strains and then smooth but significant softening as the deformation progresses. Note further
 462 that for $L = 1$ no LOE (open circles on the plots) is detected. However, failure of the porous material is not
 463 excluded (see the significant drop of the material loading capacity). As already pointed out by Rice (1976),
 464 this type of localization analysis based on uniform fields only provides an upper bound for failure while the
 465 presence of more realistic geometries can lead to localization much earlier.

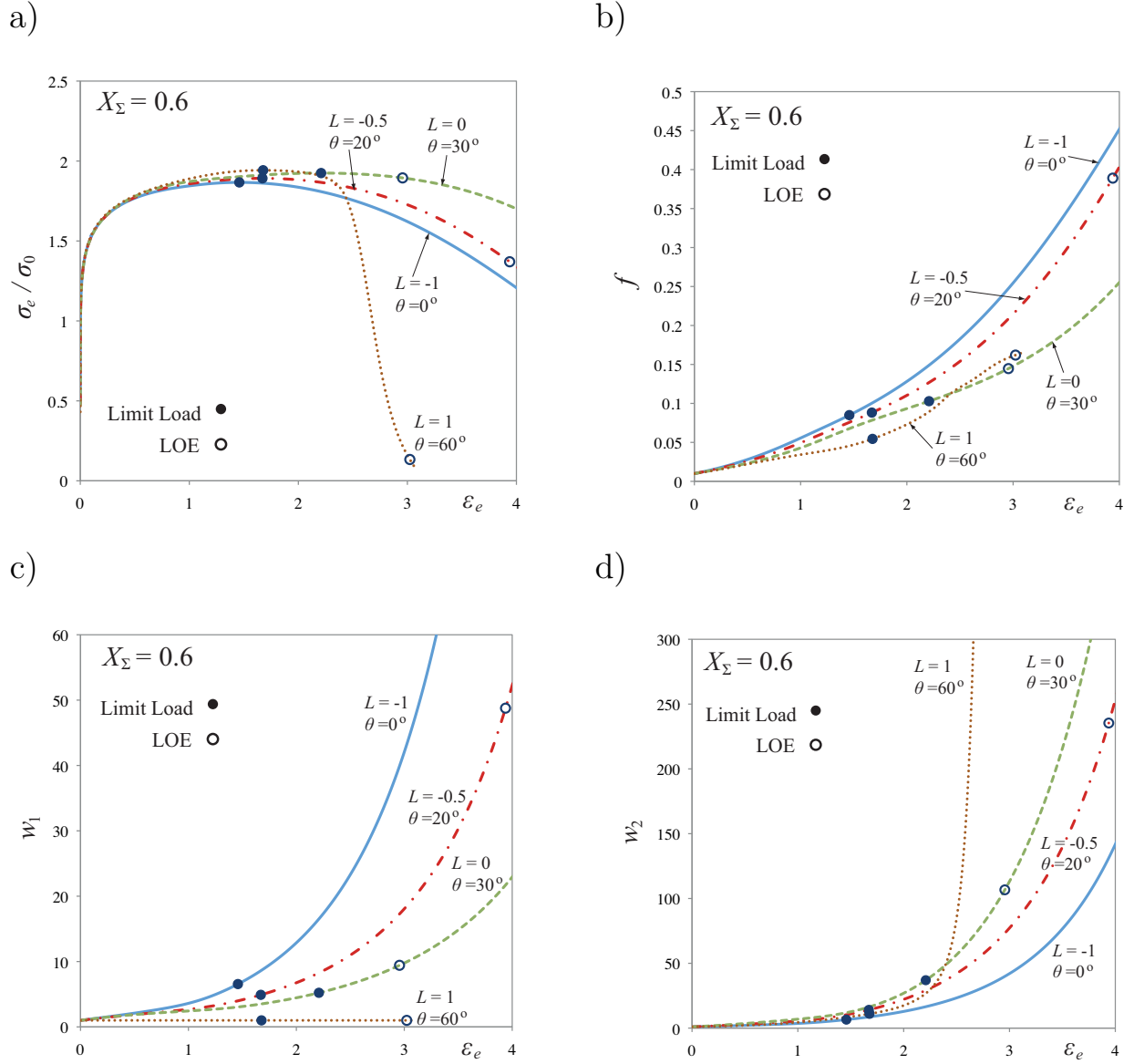


Figure 7: Plots of the SOM estimates for (a) the equivalent stress σ_e , (b) the porosity f , and the aspect ratios (c) w_1 and (d) w_2 as a function of the equivalent strain ε_e , for a moderate value of the stress triaxiality ($X_\Sigma = 0.6$) and four values of the Lode parameter. The influence of the Lode parameter is significant in this case of moderate triaxiality indicating a transition mechanism from void collapse-dominated response for $L = 1$ to porosity-dominated response for $L \leq 0$. The strain hardening exponent is $N = 0.1$ and the initial porosity $f_0 = 1\%$.

466 The fact that the stress-strain curve is independent of the Lode parameter at $X_\Sigma = 1$ is easily explained
467 by referring to Fig. 6b, where the increase of porosity is significant for all values of the Lode parameter ($L =$
468 $-1, -0.5, 0, 1$). In addition, looking at parts (c) and, especially, (d), we note that the void shape still evolves
469 as a function of ε_e , but in a much weaker manner than for the previous case of $X_\Sigma = 0.1$. This indicates that
470 the main softening mechanism in this high-triaxiality situation ($X_\Sigma = 1$) is clearly the evolution of porosity
471 which is found to lead to significant softening of the effective response of the porous material. Note that this
472 void-growth mechanism is expected to eventually lead to (three-dimensional) coalescence of the voids, and

473 failure consistent with the deep dimples observed in the micrographs shown in Fig. 1d from the experimental
 474 results of Barsoum and Faleskog (2007a). Also, it is clear that the dominance of the evolution of porosity will
 475 prevail at larger stress triaxialities $X_\Sigma > 1$ not shown here (but see Danas and Ponte Castañeda (2009b)).

476 Fig. 7 shows plots of σ_e , f , w_1 and w_2 as a function of the equivalent strain ε_e for several values of the
 477 Lode parameter ($L = -1, -0.5, 0, 1$) and a moderate value of the stress triaxiality ($X_\Sigma = 0.6$). As can be
 478 observed in part (a), for $L = -1, -0.5, 0$, the stress curves reach a maximum (limit load) and then smoothly
 479 decrease, leading to overall softening for larger values of the strain ε_e . On the other hand, the $L = 1$ curve
 480 exhibits a sharp decrease of σ_e , albeit less dramatic than the corresponding one for $X_\Sigma = 0.1$. Moreover, it
 481 is interesting to note that the limit load occurs at lower ε_e when $L = -1$ than when $L = -0.5$ or $L = 0$. In
 482 fact, as L increases to the value of 0, the critical strain ε_e at which the limit load occurs increases, whereas it
 483 decreases again as we increase further L toward the value of 1. This non-monotonic dependence on the Lode
 484 parameter L can be understood by considering the evolution of the microstructure shown in parts (b),(c)
 485 and (d) of Fig. 7. In Fig. 7b, the porosity increases for all values of L , with the weakest growth observed
 486 for $L = 1$ and the strongest for $L = -1$ (reaching relatively high values at this last case). In turn, in part
 487 (c), w_1 increases similarly to the previous case of $X_\Sigma = 0.1$. In Fig. 7d, considering $L = -0.5, 0$, we find
 488 that w_2 does not exhibit the sharp increase observed in Fig. 5d for $X_\Sigma = 0.1$ (for the same values of L).
 489 This explains the smooth softening (gentle decrease of σ_e) of the porous material observed in the curves of
 490 part (a), for $L = -1, -0.5$, and 0. By contrast, when $L = 1$, w_2 increases sharply attaining very high values
 491 corresponding to void collapse, leading to a sharp drop of the stress (similar to the corresponding case for
 492 $X_\Sigma = 0.1$). This example reveals that at moderate values of the stress triaxiality (e.g., $X_\Sigma = 0.6$) there is
 493 a transition from softening induced by *void growth* for $L = -1, -0.5$ to failure induced by *void collapse* for
 494 $L = 1$, while for $L = 0$ the failure mechanism is a combination of both void shape and porosity effects.

495 3.3. Limit load and loss of ellipticity failure curves

496 The purpose of this section is to analyze and summarize the effect of the stress triaxiality and the
 497 Lode parameter on the limit load and LOE failure instabilities. For completeness, the predictions of the
 498 present “second-order” model (SOM) will be compared and contrasted with the corresponding predictions of
 499 the recently proposed phenomenological model of Nahshon and Hutchinson (2008), labeled here as MGUR,
 500 which is based on an empirical modification of the well-known Gurson (1977) model. The MGUR model
 501 requires the choice of the parameter k_ω (see expression (10) in the referenced publication for the definition
 502 of k_ω) which is directly related to the Lode parameter. For the identification of this parameter several
 503 experiments have been performed indicating a value of k_ω between 1 and 3. In our study, we make the
 504 choice $k_\omega = 2.5$, without insisting on the quantitative aspects of the results, but rather on their qualitative
 505 nature.

506 Figure 8 shows plots of the SOM and MGUR predictions for the critical equivalent plastic strain ε_e^p
 507 attained at the limit load (i.e., the maximum in the $\sigma_e - \varepsilon_e$ curve, or equivalently, the critical hardening
 508 rate $H = 0$), as a function of the stress triaxiality X_Σ , for fixed values of the Lode parameter L (or Lode
 509 angle θ). As depicted in Fig. 8a, for fixed values of L , the SOM predictions clearly exhibit two regimes,
 510 a low-triaxiality regime where the material ductility increases with increasing triaxiality, followed by a
 511 second, high-triaxiality regime with the opposite trend. The two regimes are separated by a rather abrupt
 512 transition, or “high-ductility peak”, and as already pointed out, in the low-triaxiality regime, the source
 513 of the instability is void collapse, while in the second, it is void growth. In addition, the high-triaxiality
 514 regime is rather insensitive to the Lode parameter, while the low-triaxiality regime and the transition
 515 between the two is strongly dependent on the Lode parameter, with the ductility increasing from a value of
 516 $L = +1$ to the value of $L = -1$ (where no void collapse is possible and therefore no low-triaxiality regime is
 517 observed). In this connection, the predictions of the SOM model for failure at the limit load appear to be
 518 qualitatively consistent with the experimental results of Barsoum and Faleskog (2007a), presented in Fig.
 519 1a. Note, however, that in the results of Fig. 1a, the stress triaxiality evolves (and is non-uniform) during
 520 the deformation process as a consequence of the complex geometry of the experimental setup, and, hence,
 521 comparisons of the SOM results (which involve uniform fields and fixed triaxiality) with the experimental
 522 results of Barsoum and Faleskog (2007a) can only be qualitative in nature.

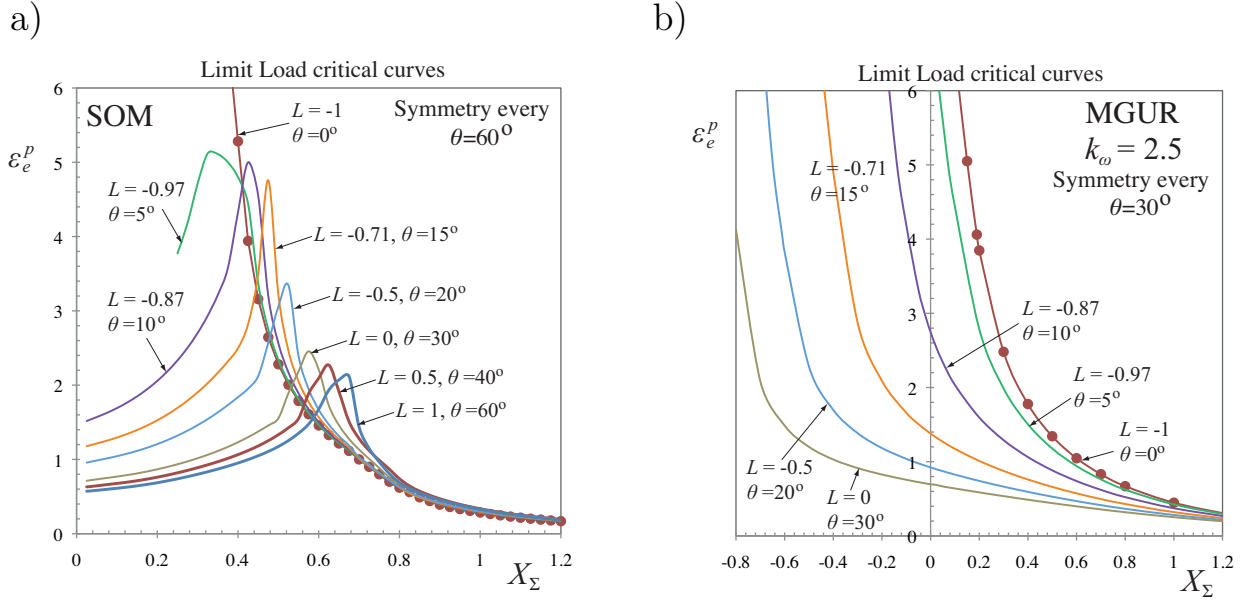


Figure 8: Limit load failure curves as predicted by (a) the SOM model and (b) the MGUR model with $k_\omega = 2.5$, as a function of the stress triaxiality X_Σ and the Lode parameter L (or θ). The critical equivalent plastic strain ε_e^p at the limit load where the hardening rate $H = 0$ provides a “macroscopic” measure of the overall ductility of the material. The strain hardening exponent is $N = 0.1$ and the initial porosity $f_0 = 1\%$.

523 By contrast, as shown in Fig. 8b, the MGUR model predictions exhibit qualitatively different behavior
524 for the limit load failure curves. As expected from the way in which it was constructed, the limit load
525 curves depend strongly on the Lode parameter, but in a manner that is monotonic with respect to the
526 triaxiality and therefore does not exhibit the two different regimes and particularly the high-ductility peaks
527 predicted by the SOM model and shown by the experimental results in Fig. 1a. This significant difference
528 found between these two models is clearly linked to the fact that the SOM model can account for void
529 shape changes and therefore can capture the void collapse mechanism contrary to the MGUR model which
530 assumes spherical void shapes during the entire deformation process. In addition, the MGUR predictions
531 for the limit load exhibit a symmetry of $\theta = 30^\circ$, implying in particular that the limit loads for $L = -1$
532 (corresponding to uniaxial tension) and $L = 1$ (biaxial tension with uniaxial compression) are identical. This
533 result is a direct consequence of the ad-hoc quadratic character of the dependence of the MGUR model on
534 the Lode parameter (see relation (4) in Nahshon and Hutchinson (2008)), and is in sharp contrast with the
535 SOM model which, for low triaxiality, predicts low ductility for $L = 1$, but very high ductility for $L = -1$.
536 It is also worth noting that the MGUR model predicts the existence of limit loads for negative values of
537 the stress triaxialities. This is also in contrast with the the SOM model which predicts that the hardening
538 produced by the porosity reduction with negative triaxialities completely overwhelms any softening due to
539 changes in the shape of the voids, and therefore the material continues to harden all the way up to complete
540 void closure.

541 Figure 9 shows SOM and MGUR predictions for the critical equivalent plastic strain ε_e^p at localization of
542 the deformation, or loss of ellipticity (LOE), defined by condition (18), as functions of the stress triaxiality
543 X_Σ , for several values of the Lode parameter L (or Lode angle θ). As shown in Fig. 9a, the SOM predictions
544 for LOE are roughly similar to those for the limit load depicted in Fig. 8a, and also exhibit two sharply
545 separated regimes. However, in addition to the strong dependence in the Lode angle observed in the low-
546 triaxiality regime, there is also some (smaller) sensitivity in the high-triaxiality regime with the ductility
547 decreasing as the value of L is increased from -1 . In fact, no LOE is detected for values of $L > 0$ and
548 $X_\Sigma > 0.5 - 0.7$, but note that the stress drops to zero for sufficiently high deformation as a consequence of

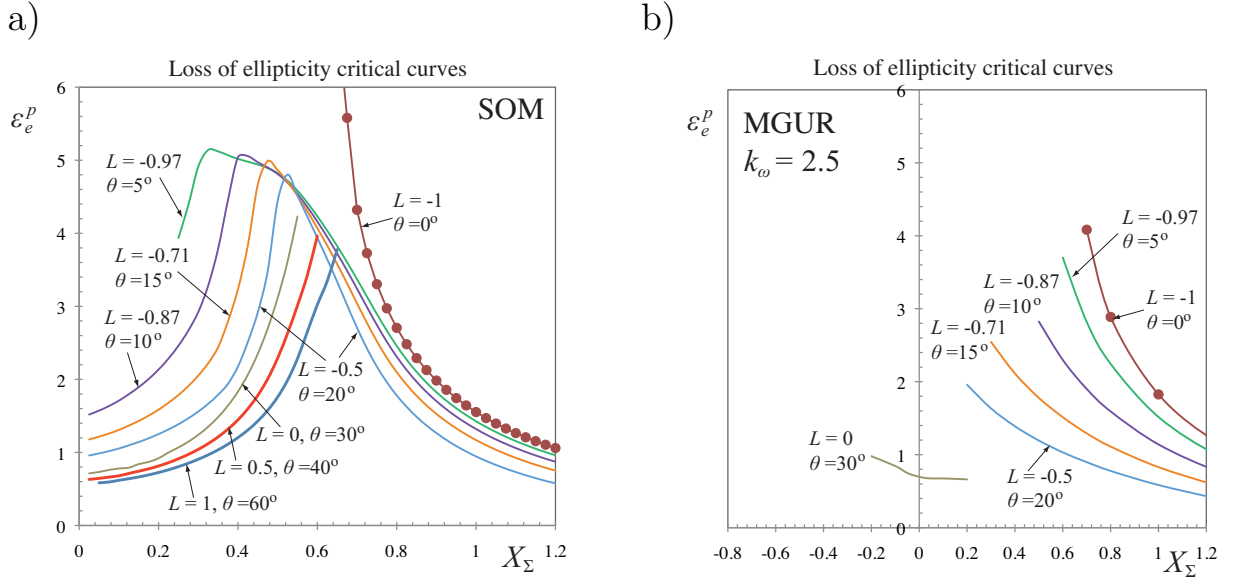


Figure 9: Loss of ellipticity failure curves as predicted by (a) the SOM model and (b) the MGUR model with $k_\omega = 2.5$, as a function of the stress triaxiality X_Σ and the Lode parameter L (or θ). The critical equivalent plastic strain ε_e^p at loss of ellipticity, with localization of deformation into dilatant shear bands taking place, provides an alternative “macroscopic” measure of the overall ductility of the material. The strain hardening exponent is $N = 0.1$ and the initial porosity $f_0 = 1\%$.

549 the continued porosity growth discussed in the previous section, while other well-known failure mechanisms
 550 such as high-triaxiality void coalescence are present (see review work of [Benzerga and Leblond \(2010\)](#)).

551 On the other hand, as shown in Fig. 9b, the MGUR model predicts LOE only for values of $L \leq 0$, while
 552 no LOE is detected for $L > 0$ (for all stress triaxialities X_Σ). Furthermore, contrary to the corresponding
 553 SOM predictions, no LOE is detected for low triaxialities except for a small branch for $L = 0$. This is
 554 a direct consequence of the fact that the MGUR model remains isotropic during the entire deformation
 555 process as a result of no void shape changes, and therefore completely misses the morphological anisotropy
 556 developed due to the significant void shape evolution in the low-triaxiality regime. Finally, it is noted in the
 557 context of this figure that for the special values of $L = 1$ and -1 , the MGUR model reduces to the Gurson
 558 model and note that the predictions for LOE for these two values are different (in one case there is LOE
 559 and in the other there is not), which in view of the identical predictions for the limit load for these two cases
 560 demonstrates the sensitivity of the LOE condition to the pertinent kinematical conditions.

561 Finally, in Fig. 10, the earlier LOE results are completed by depicting the orientation of the localization
 562 band in terms of the angle φ that defines the orientation of the normal to the band \mathbf{n} with respect to the x_2
 563 axis (see inset sketches in the plots). The SOM and the MGUR results are shown in Fig. 10a and Fig. 10b,
 564 respectively, as a function of the stress triaxiality X_Σ for several values of the Lode parameter L (or Lode
 565 angle θ). The complementary angle φ_g , associated with the vector \mathbf{g} , which controls the type of deformation
 566 inside the band, is found to be $\varphi_g = -\varphi$ for both the SOM and the MGUR models. Moreover, note that
 567 the normal to the band \mathbf{n} , as predicted by both the SOM and the MGUR models, lies on the $x_2 - x_3$ plane.
 568 In particular, for the case when $\varphi = -\varphi_g = 45^\circ$ (i.e., $\mathbf{n} \perp \mathbf{g}$), the state of deformation inside the band is
 569 a simple shear and thus formation of a shear localization band is produced. This is the case for $L \geq 0$ (or
 570 $\theta \geq 30^\circ$) for the SOM model and $L = 0$ (or $\theta = 30^\circ$) for the MGUR model. Note that, in accord with
 571 the earlier discussions, the MGUR model predicts no loss of ellipticity for $L > 0$ and hence no angles are
 572 shown for these cases. On the other hand, for $L < 0$, we observe for both the SOM and the MGUR models
 573 that the predicted localization band angle is smaller than 45° and hence the state of deformation inside the

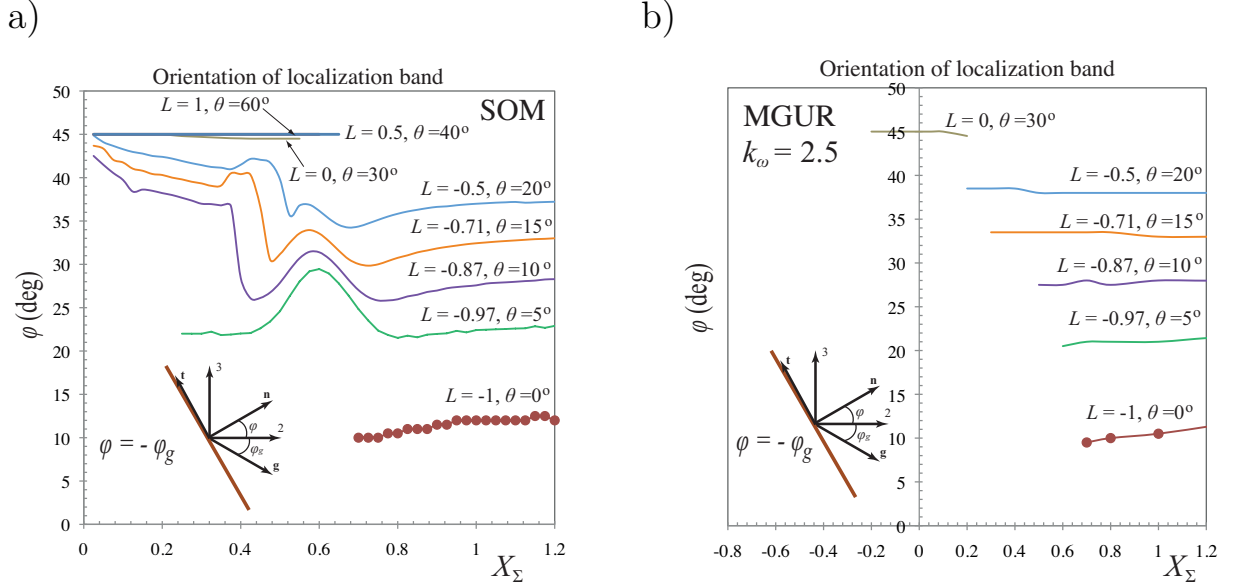


Figure 10: Orientation of the localization band defined by the angle φ as predicted by (a) the SOM model and (b) the MGUR model with $k_\omega = 2.5$, as a function of the stress triaxiality X_Σ and the Lode parameter L (or θ). The strain hardening exponent is $N = 0.1$ and the initial porosity $f_0 = 1\%$.

574 band is a combination of shear plus dilatation across the band (in the direction of the normal to the band).
 575 The lowest value for φ is attained in both models for $L = -1$, where the localization band is found to be at
 576 an angle of about 10° . It should be emphasized that at large triaxialities the SOM and the MGUR models
 577 predict very similar localization angles, highlighting once again the fact that the main difference between
 578 the models is for low triaxialities when changes in the shape of the pores become possible.

579 3.4. Influence of strain hardening exponent and initial porosity on failure curves

580 Making use of the SOM model, a parametric study is carried out to investigate the effect of the strain
 581 hardening exponent of the matrix phase and the initial porosity on the limit load and loss of ellipticity (LOE)
 582 failure curves. Thus, the following figures show plots of the critical equivalent plastic strain ε_e^p attained at
 583 the limit load (i.e., maximum in the $\sigma_e - \varepsilon_e$ curve, or equivalently critical hardening rate $H = 0$), and at
 584 loss of ellipticity (LOE), or localization of deformation (given by (18)), as functions of the stress triaxiality
 585 X_Σ and the Lode parameter L (or Lode angle θ).

586 Figure 11 shows limit load maps for (a) $L = -1$, (b) $L = -0.5$, (c) $L = 0$ and (d) $L = 1$ as a function of the
 587 stress triaxiality X_Σ using different strain hardening exponents for the matrix phase, $N = 0.01, 0.05, 0.1, 0.2$.
 588 (Note that $N = 0$ and $N = 1$ correspond to ideally plastic and linear hardening behaviors, respectively.) The
 589 limit load failure curves are strongly dependent on N for moderate and high triaxialities such as $X_\Sigma > 0.4$,
 590 as observed in all parts of Fig. 11. By contrast, at low stress triaxialities ($X_\Sigma < 0.35$) and $L > -1$, i.e.,
 591 Fig. 11b,c,d, the limit load failure curves exhibit negligible dependence on the strain hardening exponent.
 592 This is due to the fact that at low X_Σ , the limit load occurs in such an abrupt manner due to the very
 593 fast void shape changes (observed in the context of Fig. 5) that the hardening of the matrix plays almost
 594 no role on the overall softening mechanism of the porous material. On the other hand, as the triaxiality
 595 increases the growth of porosity dominates the limit load mechanism. The porosity growth however is
 596 rather smooth allowing the strain hardening exponent to play a dominant role on the overall softening of the
 597 material. In contrast, as shown in Fig. 12, the strain hardening exponent N has only a negligible effect on
 598 the LOE predictions. This suggests that once the material enters the softening regime, kinematics controls
 599 the localization mechanism and hence the effect of N is not important.

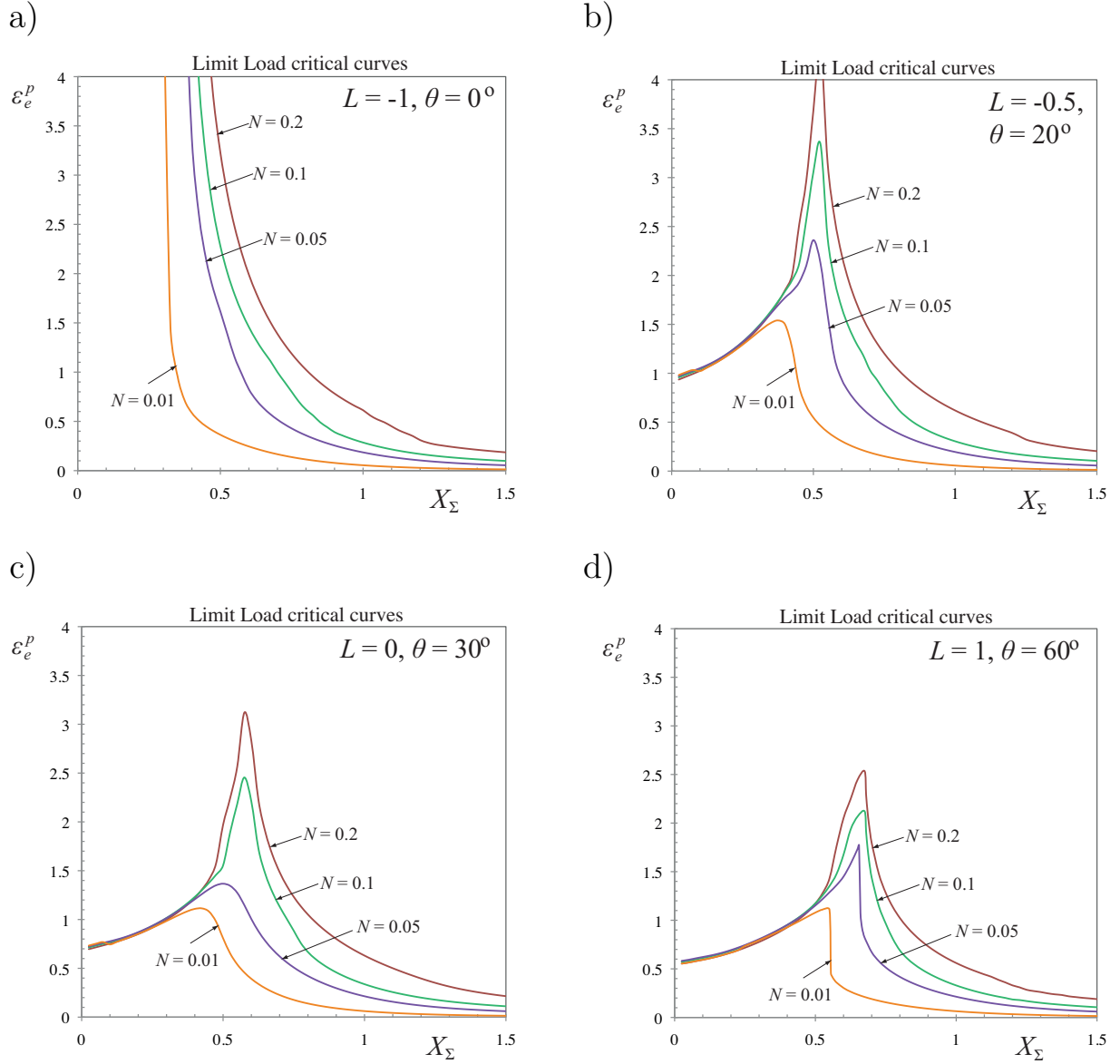


Figure 11: SOM limit load failure curves as a function of the stress triaxiality X_Σ and the strain hardening exponent $N = 0.01, 0.05, 0.1, 0.2$ for various values of the Lode parameter: (a) $L = -1$, (b) $L = -0.5$, (c) $L = 0$ and (d) $L = 1$. The initial porosity $f_0 = 1\%$.

600 Fig. 13 shows the limit load failure curves as a function of the stress triaxiality X_Σ for different initial
601 porosities $f_0 = 0.1, 1, 5\%$ and Lode parameters: (a) $L = -1$, (b) $L = -0.5$, (c) $L = 0$ and (d) $L = 1$.
602 Overall, an effect is observed especially near the transition from the low- to the high-triaxiality regimes,
603 which becomes less sharp with decreasing porosity. It should also be noted that higher initial porosities f_0
604 lead to a reduction in ductility, as determined by the limit load, except in the transition regime, where the
605 opposite trend is observed. Finally, Fig. 14 presents LOE critical curves as a function of the stress triaxiality
606 X_Σ for different initial porosities $f_0 = 0.1, 1$, and 5% and Lode parameters: (a) $L = -1$, (b) $L = -0.5$, (c)
607 $L = 0$ and (d) $L = 1$. The effect of f_0 on the LOE failure curves is non-negligible contrary to the effect
608 of the strain hardening exponent N shown in Fig. 12. As observed here, higher initial porosity f_0 leads to

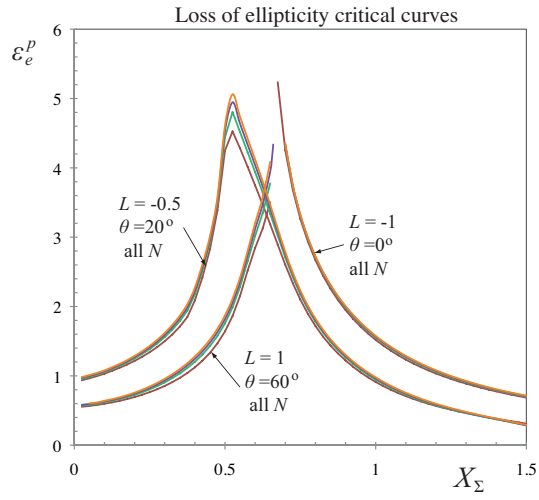
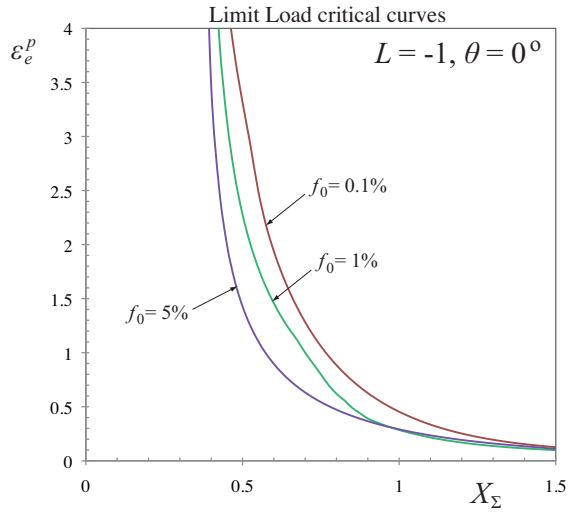


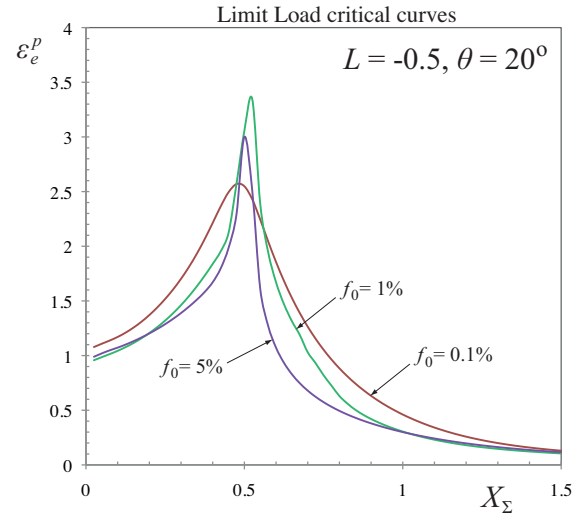
Figure 12: SOM loss of ellipticity (LOE) failure curves as a function of the stress triaxiality X_Σ and the strain hardening exponent $N = 0.01, 0.05, 0.1, 0.2$ for various values of the Lode parameter: $L = -1, -0.5, 1$. The initial porosity $f_0 = 1\%$.

609 lower critical strains for localization, at least for the range of porosities considered in this study.

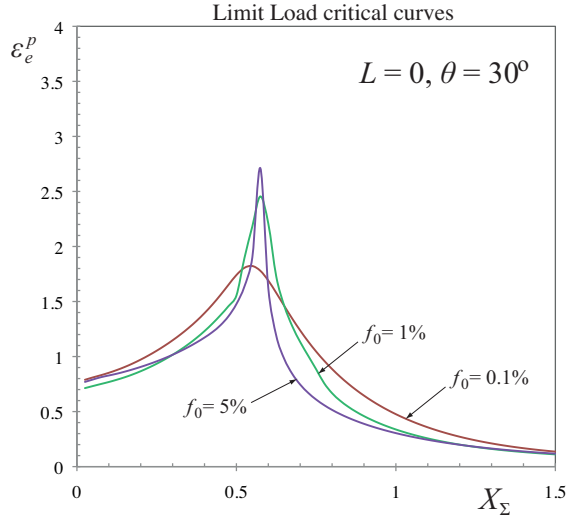
a)



b)



c)



d)

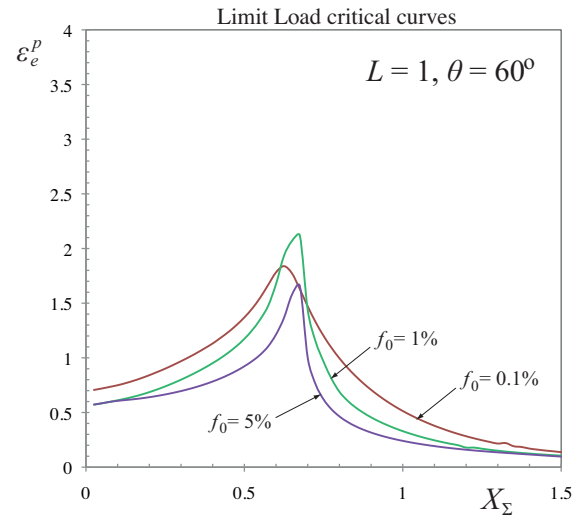


Figure 13: SOM limit load failure curves as a function of the stress triaxiality X_Σ and the initial porosity $f_0 = 0.1, 15\%$ for various values of the Lode parameter: (a) $L = 1$, (b) $L = -0.5$, (c) $L = 0$ and (d) $L = 1$. The strain hardening exponent is $N = 0.1$.

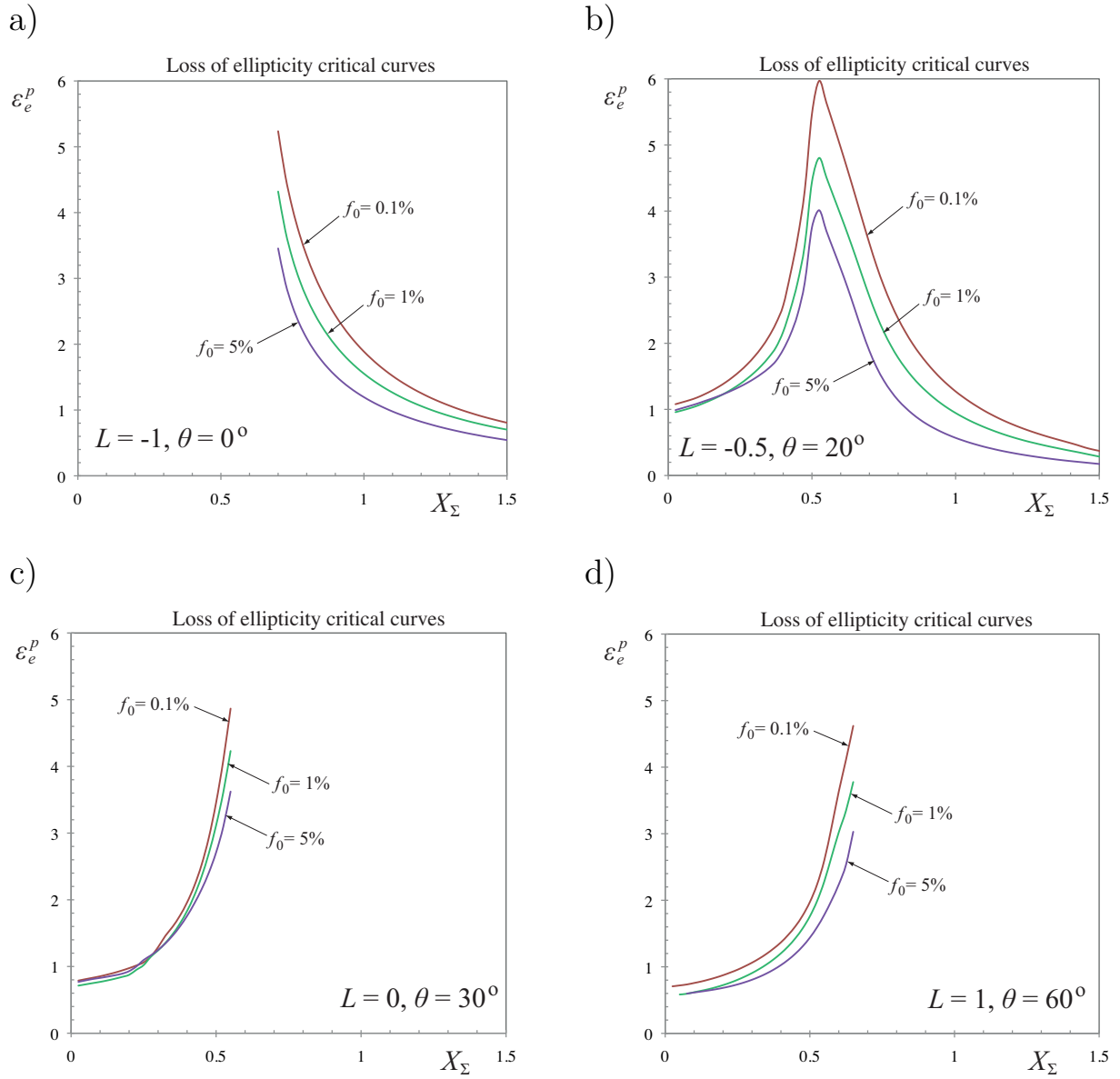


Figure 14: SOM loss of ellipticity failure curves as a function of the stress triaxiality X_Σ and the initial porosity $f_0 = 0.1, 15\%$ for various values of the Lode parameter: (a) $L = 1$, (b) $L = -0.5$, (c) $L = 0$ and (d) $L = 1$. The strain hardening exponent is $N = 0.1$.

610 4. Conclusions and perspectives

611 In this work, we have investigated the influence of the stress triaxiality and the Lode parameter on
612 the failure of elasto-plastic porous materials subjected to macroscopically uniform, triaxial loadings. For
613 this purpose, we have made use of a recently developed “second-order” nonlinear homogenization model
614 (SOM) of [Danas and Ponte Castañeda \(2009a\)](#), which can account for the effects of void shape and porosity
615 evolution on the overall softening/hardening response of the porous material. Material failure of the porous
616 ductile solid has been modeled by means of two different macroscopic criteria: (i) vanishing of the overall
617 hardening rate ($H = 0$), corresponding to the existence of limit load, or maximum stress in the constitutive
618 response of the material, and (ii) loss of ellipticity of the incremental response of the material corresponding
619 to localization of the deformation into dilatant shear bands due to the compressible overall response of the
620 porous material ([Rice, 1976](#)).

621 The main finding of this work is that failure can occur by two very different mechanisms at high- and
622 low-triaxiality. In agreement with well-established results, at high triaxialities, the model predicts significant
623 *void growth* leading to a softening effect which eventually overtakes the intrinsic strain hardening of the solid
624 material and produces overall softening. Thus, a limit load is reached at a critical strain that decreases with
625 increasing triaxiality and is found to be independent of the Lode parameter. This limit load point is then
626 followed by a significant reduction in the load-carrying capacity of the material and loss of ellipticity (at
627 least for negative values of the Lode parameter). On the other hand, at low triaxialities, the model predicts
628 *void collapse* due to an abrupt flattening of the initially spherical voids with *decreasing* porosity, which
629 in turn leads to a sharp drop in the load-carrying capacity of the porous solid. The precise value of the
630 strain at the onset of the instability, which determines the overall ductility of the material, depends on
631 the competition of the hardening produced by the reduction of the porosity and the softening due to the
632 change in shape of the pores, and is highly sensitive to the value of the Lode parameter. Thus, for biaxial
633 tension with axisymmetric compression ($L = 1$), the onset of the limit load instability, as well as the loss
634 of ellipticity shortly thereafter, decreases as the triaxiality is reduced toward zero, while for axisymmetric
635 tension ($L = -1$) no void collapse is possible and therefore no instability is observed for small values of
636 the triaxiality. Moreover, for fixed, small values of the triaxiality ($X_\Sigma < 0.6$), the ductility of the porous
637 material decreases as the value of the Lode parameter increases from -1 to $+1$. In addition, a sharp
638 transition is observed as the failure mechanism switches from void collapse to void growth for intermediate
639 values of the stress triaxiality ($0.3 < X_\Sigma < 0.7$), depending strongly on the value of the Lode parameter
640 and leading to high-ductility peaks in the failure maps. In this regard, the theoretical predictions are found
641 to be in qualitative agreement with recent experimental observations by [Barsoum and Faleskog \(2007a\)](#) and
642 [Dunand and Mohr \(2010\)](#), even though it should be emphasized that the stress and deformation fields are
643 not uniform and that the values of the triaxiality and Lode parameter are not controlled independently in
644 these experiments. In this sense, the theoretical predictions presented in this work suggest the critical need
645 for new experiments with improved control over the uniformity of the stress and strain fields, as well as the
646 loading conditions.

647 The predictions of the second-order model have been compared with the corresponding results of the *ad*
648 *hoc* modification of the Gurson model, MGUR, proposed by [Nahshon and Hutchinson \(2008\)](#), and significant
649 differences have been identified. First and foremost, the MGUR model cannot capture void collapse, because
650 the voids are assumed to remain spherical throughout the deformation. Because of this, while it is possible
651 to artificially soften the material response by introducing a dependence on the Lode angle, the failure curves
652 still increase with decreasing triaxiality into the negative triaxiality regime. In addition, in contrast with the
653 second-order predictions, the effect of the Lode parameter on the maximum load is symmetric with respect
654 to the sign of the Lode angle, and does not lead to loss of ellipticity for most values of the Lode parameter
655 in the low-triaxiality regime. In this connection, it is important to emphasize that the relevance of the Lode
656 angle is not so much through its direct effect on the macroscopic yield surface, which is relatively small, but
657 instead through its much more significant implications for the evolution of the microstructure, especially
658 when changes in the shape of the voids are allowed. Indeed, this ability to account for the very different
659 and generally strongly anisotropic evolution of the microstructure of the material at fixed, low values of the
660 stress triaxiality, but with different Lode parameters ranging from axisymmetric tension ($L = +1$) to biaxial

661 tension with axisymmetric compression ($L = -1$), is the main advantage of the SOM model over the models
662 of Gurson (1977), Nahshon and Hutchinson (2008) and Nielsen and Tvergaard (2010).

663 For completeness, the SOM model has also been used to investigate the possible effects of the matrix
664 strain-hardening exponent N and the initial porosity f_0 . We have found that the strain-hardening exponent
665 N has a significant effect on the limit load for stress triaxialities $X_\Sigma > 0.4$, and consequently the location
666 of the transition from the void collapse to the void growth mechanisms. In contrast, it has only a negligible
667 effect on the limit load at low stress triaxialities, due to the abruptness of the void collapse mechanism in
668 this case, leading to strong material softening. On the other hand, the strain hardening exponent affects
669 only slightly the loss of ellipticity curves. In turn, different initial porosities f_0 have an effect on both the
670 limit load and loss of ellipticity failure curves. Higher initial porosities lead, in general, to lower critical
671 strains for the limit load and loss of ellipticity, except for the limit load curves in the transition region
672 ($0.4 < X_\Sigma < 0.6$), where the opposite trend is observed.

673 It should also be emphasized that this work deals only with instabilities at the material level and that no
674 actual macroscopic geometries have been considered. Nonetheless, the instability results obtained assuming
675 that macroscopically uniform fields are present in a given specimen should correspond to “material instabili-
676 ties,” and provide a loose upper bound for the resistance of the material to ductile failure under more general
677 loading conditions (Rice, 1976). In this connection, it is also relevant to mention that the three-dimensional
678 studies of Barsoum and Faleskog (2007b, 2011) and the corresponding two-dimensional studies of Tvergaard
679 (2009) in two-dimensions, seem to suggest that void rotations may somehow be necessary for low-triaxiality
680 failure. However, the results of the present work for triaxial loading conditions (with fixed loading axes)
681 show that while void rotations may enhance (or reduce) the ductility of the material, void rotations are not
682 strictly necessary for material instabilities (of the maximum load, or loss of ellipticity type) at low-triaxiality,
683 since the basic micro-mechanism of void collapse does not require them. In any event, void rotations can
684 easily be handled by the general version of the SOM model (Danas and Ponte Castañeda, 2009a), and this
685 will be pursued in future work. Interestingly, Kailasam and Ponte Castañeda (1997) have shown (refer
686 to Fig. 2 in that reference) using an earlier version of the model (Ponte Castañeda and Zaidman, 1994;
687 Kailasam and Ponte Castañeda, 1998) that the effective hardening rate of a porous rigid-plastic material
688 subjected to simple shear can become zero as a consequence of the combined effects of the changes in shapes
689 and orientation of the voids.

690 It should also be remarked that the larger issue of how to proceed after (local) loss of ellipticity
691 in the analysis of an actual structural problem is still a largely open issue. However, it is clear that
692 more general and reliable models, as well as estimates for their loss of ellipticity, are essential for further
693 progress, as are finite element implementations of such models in order to be able to handle the non-uniform
694 fields that would be expected to develop under actual experimental conditions. In this latter connection,
695 it should be mentioned that such implementations are already available (see Kailasam et al. (2000) and
696 Aravas and Ponte Castañeda (2004)) for the earlier “variational” framework of Ponte Castañeda and Zaidman
697 (1994). In addition, a numerical implementation of an improved version of the “variational” framework,
698 which provides more accurate results for both low and high stress triaxialities has been developed—and im-
699 plemented for three-dimensional experimental geometries—recently by Danas and Aravas (in preparation).

700 As a final remark, it should be mentioned that an additional advantage in the use of a homogeniza-
701 tion approach for porous and other heterogeneous solids is its generality. Thus, for example, the effect
702 of anisotropy in the matrix can be accounted for in a straightforward fashion by treating this phase as
703 a polycrystalline aggregate and using the second-order homogenization method (Liu and Ponte Castañeda,
704 2004) consistently to estimate the overall response including both the effects of porosity and crystallographic
705 texture. A first step in this direction is presented in the recent work of Lebensohn et al. (2011), which opens
706 up the possibility of modeling the simultaneous effects of porosity and texture evolution on the overall re-
707 sponse and stability of porous polycrystalline solids, which is expected to be especially important for porous
708 low-symmetry metals, such as porous Ti and Mg alloys.

709 It is also relevant to mention in this connection that the second-order homogenization method has been
710 used successfully to estimate loss of ellipticity in porous elastomers (Lopez Pamies and Ponte Castañeda,
711 2007a; 2007b). Although the failure maps are very different for this case, comparisons with careful numerical
712 calculations (Michel et al., 2007) show that the model indeed has the capability of capturing not only the

713 overall macroscopic behavior, but also the possible onset of “macroscopic” instabilities, such as loss of
714 ellipticity (Geymonat et al., 1993).

715 Acknowledgments

716 K.D. would like to acknowledge the support of the Engineering Department, Cambridge University, where
717 parts of this work were carried out, as well as of the Solid Mechanics Laboratory of the Ecole Polytechnique.
718 P.P.C would like to acknowledge partial support by the National Science Foundation under Grant Number
719 CMMI-0969570.

720 References

- 721 Anderson, P.M., Fleck, N.A., Johnson, K.L., 1990. Localization of plastic deformation in shear due to microcracks. *J. Mech.*
722 *Phys. Solids* 38, 681–699.
- 723 Aravas, N., Ponte Castañeda, P., 2004. Numerical methods for porous metals with deformation-induced anisotropy. *Comput.*
724 *Methods Appl. Mech. Engrg.* 193, 3767–3805.
- 725 Bao, Y., Wierzbicki, T., 2004. On fracture locus in the equivalent strain and stress triaxiality space. *Int. J. Mech. Sci.* 46 (81),
726 81–98.
- 727 Barsoum, I., Faleskog, J. 2007a. Rupture mechanisms in combined tension and shear Experiments. *Int. J. Solids Struct.*, 44,
728 1768–1786.
- 729 Barsoum, I., Faleskog, J. 2007b. Rupture mechanisms in combined tension and shear Micromechanics. *Int. J. Solids Struct.*,
730 44, 5481–5498.
- 731 Barsoum, I., Faleskog, J. 2011. Micromechanical analysis on the influence of the Lode parameter on void growth and coalescence.
732 *Int. J. Solids Struct.*, 48, 925–938.
- 733 Benzerga, A. A., 2002. Micromechanics of coalescence in ductile fracture. *J. Mech. Phys. Solids* 50, 1331–1362.
- 734 Benzerga, A. A., Besson, J., Pineau, A., 1999. Coalescence-Controlled Anisotropic Ductile Fracture *J. Engin. Mater. Tech.*,
735 121, 221–229
- 736 Benzerga, A. A., Leblond, J.-B., 2010. Ductile Fracture by Void Growth to Coalescence. *Adv. Appl. Mech.* 44, 170–297.
- 737 Budiansky, B., Hutchinson, J. W., Slutsky, S., 1982. Void growth and collapse in viscous solids. *Mechanics of Solids, The*
738 *Rodney Hill 60th anniversary Volume*, Hopkins, H. G. and Sewell, M. J., eds., Pergamon Press, Oxford, 13–45.
- 739 Chu, C.C., Needleman, A., 1980. Void nucleation effects in biaxially stretched sheets. *J. Engrg. Mat. Tech.* 102, 249–256.
- 740 Dafalias, Y., F., 1985. The plastic spin. *J. Appl. Mech.* 52, 865–871.
- 741 Danas, K., 2008. Homogenization-based constitutive models for viscoplastic porous media with evolving microstructure. Ph.D.
742 thesis, LMS, École Polytechnique: <http://www.polymedia.polytechnique.fr/Center.cfm?Table=These>.
- 743 Danas, K., Aravas, N., Numerical modeling of elasto-plastic porous materials with void shape effects at finite deformations, in
744 preparation.
- 745 Danas, K., Idiart, M.I., Ponte Castañeda, P., 2008a. Homogenization-based constitutive model for two-dimensional viscoplastic
746 porous media. *C. R. Mecanique* 336, 79-90.
- 747 Danas, K., Idiart, M.I., Ponte Castañeda, P., 2008b. Homogenization-based constitutive model for isotropic viscoplastic porous
748 media. *Int. J. Solids Struct.* 45, 3392–3409.
- 749 Danas, K., Ponte Castañeda, P., 2009a. A finite-strain model for anisotropic viscoplastic porous media: I - Theory. *Eur. J.*
750 *Mech. A/Solids* 28, 387–401.
- 751 Danas, K., Ponte Castañeda, P., 2009b. A finite-strain model for anisotropic viscoplastic porous media: II - Applications. *Eur.*
752 *J. Mech. A/Solids* 28, 402–416.
- 753 Dunand, M., Mohr, D., 2010. Hybrid experimental-numerical analysis of basic ductile fracture experiments for sheet metals.
754 *Int. J. Solids Struct.* 47, 1130–1143.
- 755 Duva, J. M., Hutchinson, J. W., 1984. Constitutive potentials for dilutely voided nonlinear materials. *Mech. Mater.* 3, 41–54.
- 756 Eshelby, J.D., 1957. The determination of the elastic field of an ellipsoidal inclusion and related problems. *Proc. R. Soc. Lond.*
757 *A* 241, 376–396.
- 758 Flandi, L., Leblond, J.-B., 2005a. A new model for porous nonlinear viscous solids incorporating void shape effects – I: Theory,
759 *Eur. J. Mech. A/Solids* 24, 537–551.
- 760 Flandi, L., Leblond, J.-B., 2005b. A new model for porous nonlinear viscous solids incorporating void shape effects – II:
761 Numerical validation, *Eur. J. Mech. A/Solids* 24, 552–571.
- 762 Gărăjeu, M., Michel, J.-C., Suquet, P., 2000. A micromechanical approach of damage in viscoplastic materials by evolution in
763 size, shape and distribution of voids. *Comp. Methods Appl. Mech. Engrg.* 183, 223–246.
- 764 Garrison Jr., W.M., Moody, N.R., 1987. Ductile fracture. *J. Phys. Chem. Solids* 48, 1035–1074.
- 765 Geymonat, G., Müller, S., Triantafyllidis, N., 1993. Homogenization of nonlinearly elastic materials, microscopic bifurcation
766 and macroscopic loss of rank-one convexity. *Archive for Rational Mechanics and Analysis* 122, 231–290.
- 767 Gologanu, M., Leblond, J.-B., Devaux, J., 1993. Approximate models for ductile metals containing non-spherical voids – case
768 of axisymmetric prolate ellipsoidal cavities. *J. Mech. Phys. Solids* 41, 1723–1754.
- 769 Gologanu, M., Leblond, J.-B., Devaux, J., 1994. Approximate models for ductile metals containing non-spherical voids – case
770 of axisymmetric oblate ellipsoidal cavities. *ASME J. Engrg. Materials Technol.* 116, 290–297.

- 771 Gologanu, M., Leblond, J.-B., Devaux, J., 1997. Recent extensions of Gurson's model for porous ductile metals. Suquet, P.
772 (Ed.), Continuum micromechanics. In: CISM lectures series. Springer, New York, 61–130.
- 773 Gurson, A.L., 1977. Continuum theory of ductile rupture by void nucleation and growth. *J. Engng. Mater. Technol.* 99, 2–15.
- 774 Hancock, J.W., Mackenzie, A.C., 1976. On the mechanisms of ductile fracture in high-strength steels subject to multi-axial
775 stress-states. *J. Mech. Phys. Solids* 24, 147–160.
- 776 Johnson, G.R., Cook, W.H., 1985. Fracture characteristics of three metals subjected to various strains, strain rates, tempera-
777 tures and pressures. *Engrg. Fracture Mech.* 21 (1), 31–48.
- 778 Kailasam, M., Aravas, N., Ponte Castañeda, P. 2000. Porous metals with developing anisotropy: Constitutive models, compu-
779 tational issues and applications to deformation processing. *Computer Modeling in Engineering and Sciences* 1, 105–118.
- 780 Kailasam, M., Ponte Castañeda, P., 1997. The evolution of anisotropy in porous materials and its implications for shear
781 localization. *IUTAM Symposium on Mechanics of Granular and Porous Materials*, N.A. Fleck and A.C.F. Cocks, Eds.,
782 Kluwer Academic Publishers, 365–376.
- 783 Kailasam, M., Ponte Castañeda, P., 1998. A general constitutive theory for linear and nonlinear particulate media with
784 microstructure evolution. *J. Mech. Phys. Solids* 46, 427–465.
- 785 Kailasam, M., Ponte Castañeda, P., and Willis, J. R., 1997a. The effect of particle size, shape, distribution and their evolution
786 on the constitutive response of nonlinearly viscous composites. I. Theory. *Phil. Trans. R. Soc. Lond. A* 355, 1835–1852.
- 787 Kailasam, M., Ponte Castañeda, P., and Willis, J. R., 1997b. The effect of particle size, shape, distribution and their evolution
788 on the constitutive response of nonlinearly viscous composites. II. Examples. *Phil. Trans. R. Soc. Lond. A* 355, 1853–1872.
- 789 Keralavarma, S.M., Benzerga, A. A., 2010. A constitutive model for plastically anisotropic solids with non-spherical voids. *J.*
790 *Mech. Phys. Solids* 58, 874–901.
- 791 Lebensohn, R.A., Idiart, M.I., Ponte Castañeda, P., Vincent, P.-G. 2011. Dilatational viscoplasticity of polycrystalline solids
792 with intergranular cavities. *Phil. Mag.*, published online (DOI: 10.1080/14786435.2011.561811).
- 793 Lee, B. J., Mear, M. E., 1992. Axisymmetric deformation of power-law solids containing a dilute concentration of aligned
794 spheroidal voids. *J. Mech. Phys. Solids* 40, 1805–1836.
- 795 Le Roy, G., Embury, J.D., Edwards, G., Ashby, M.F., 1981. A model of ductile fracture based on the nucleation and growth
796 of voids. *Acta Met.* 29, 1509–1522.
- 797 Lopez Pamiés, O., Ponte Castañeda, P., 2007. Homogenization-based constitutive models for porous elastomers and implications
798 for macroscopic instabilities: IAnalysis. *J. Mech. Phys. Solids* 55, 1677–1701.
- 799 Lopez Pamiés, O., Ponte Castañeda, P., , 2007. Homogenization-based constitutive models for porous elastomers and implica-
800 tions for macroscopic instabilities: IIResults. *J. Mech. Phys. Solids* 55, 1702–1728.
- 801 Liu, Y., Ponte Castañeda, P., 2004. Second-order theory for the effective behavior and field fluctuations in viscoplastic
802 polycrystals. *J. Mech. Phys. Solids* 52, 467–495.
- 803 McClintock, F. A., 1968. A criterion by for ductile fracture by growth of holes. *Trans. ASME, Series E, J. Appl. Mech.* 35,
804 363–371.
- 805 McClintock, F.A., 1971. Plasticity aspects of fracture. In: Leibowitz, H. (Ed.), *Fracture*, vol. 3. Academic Press, pp. 47–225.
- 806 Michel, J.-C., Suquet, P., 1992. The constitutive law of nonlinear viscous and porous materials. *J. Mech. Phys. Solids* 40, 783
807 – 812.
- 808 Michel, J.-C., Lopez-Pamiés, O., Ponte Castañeda, P., Triantafyllidis, N., 2007. Microscopic and macroscopic instabilities in
809 finitely strained porous elastomers. *J. Mech. Phys. Solids* 55, 900–938.
- 810 Mohr, D., Ebnoether, F., 2009. Plasticity and fracture of martensitic boron steel under plane stress conditions. *Int. J. Solids*
811 *Struct.* 46, 3535–3547.
- 812 V. Monchiet, E. Charkaluk, D. Kondo, 2007. An improvement of Gurson-type models of porous materials by using Eshelby-like
813 trial velocity fields, *C. R. Mcanique*, 335, 32–41.
- 814 Nahshon, K., Hutchinson, J. W., 2008. Modification of the Gurson model for shear failure. *Eur. J. Mechanics A/Solids* 27,
815 1–17.
- 816 Needleman, A., Rice, J.R., 1978. Limits to ductility set by plastic flow localization. In: Koistinen, D.P., et al. (Eds.), *Mechanics*
817 *of Sheet Metal Forming*. Plenum Publishing, 237–267.
- 818 Nielsen, K. L., Tvergaard, V., 2010. Ductile shear failure or plug failure of spot welds modelled by modified Gurson model.
819 *Engng. Fract. Mech.* 77, 1031–1047.
- 820 Pardoën, T., Hutchinson, J. W., 2000. An extended model for void growth and coalescence. *J. Mech. Phys. Solids* 48, 2467–2512.
- 821 Ponte Castañeda, P., 1991. The effective mechanical properties of nonlinear isotropic composites. *J. Mech. Phys. Solids* 39,
822 45–71.
- 823 Ponte Castañeda, P., 2002a. Second-order homogenization estimates for nonlinear composites incorporating field fluctuations.
824 I. Theory. *J. Mech. Phys. Solids* 50, 737–757.
- 825 Ponte Castañeda, P., 2002b. Second-order homogenization estimates for nonlinear composites incorporating field fluctuations.
826 II. Applications. *J. Mech. Phys. Solids* 50, 759–782.
- 827 Ponte Castañeda, P., Willis, J.R., 1995. The effect of spatial distribution on the effective behavior of composite materials and
828 cracked media. *J. Mech. Phys. Solids* 43, 1919–1951.
- 829 Ponte Castañeda, P., Zaidman, M., 1994. Constitutive models for porous materials with evolving microstructure. *J. Mech.*
830 *Phys. Solids* 42, 1459–1497.
- 831 Rice, J.R., Tracey, D.M., 1969. On the ductile enlargement of voids in triaxial fields. *J. Mech. Phys. Solids* 17, 201–217.
- 832 Rice, J. R. (1976). The localization of plastic deformation. *Proceedings of the 14th International Congress of Theoretical and*
833 *Applied Mechanics*, W. T. Koiter, ed., North-Holland Publishing Company, 207–220.
- 834 Teirlinck, D., Zok, F., Embury, J.D., Ashby, M.F., 1988. Fracture mechanism maps in stress space. *Acta Met.* 36 (5), 1213–1228.
- 835 Tvergaard, V., 1981. Influence of voids on shear band instabilities under plane strain conditions. *Int. J. Fracture* 17, 389–407.

- 836 Tvergaard, V., 1990. Material failure by void growth. *Adv. Appl. Mech.* 27, 83–151.
- 837 Tvergaard, V., 2009. Behaviour of voids in a shear field. *Int. J. Fracture* 158, 41–49.
- 838 Willis, J.R., 1978. Variational principles and bounds for the overall properties of composites. *Continuum Models and Discrete*
839 *Systems* 2, (ed. J. Provan), 185–212.
- 840 Willis, J.R., 1981. Variational and related methods for the overall properties of composites. *Adv. Appl. Mech.* 21, 1–78.
- 841 Willis, J.R., 1991. On methods for bounding the overall properties of nonlinear composites. *J. Mech. Phys. Solids* 39, 73–86.
- 842 Yamamoto, H., 1978. Conditions for shear localization in the ductile fracture of void containing materials. *Int. J. Fracture* 14,
843 347–365.